The Dissertation Committee for Joshua Daniel Morris Certifies that this is the approved version of the following dissertation:

Quantifying Internal Electric Fields in Organic Bulk Heterojunctions

Committee:

Katherine Willets, Co-Supervisor

Xiaoyang Zhu, Co-Supervisor

David Vanden Bout

Charles Mullins

Xiaoqin Li

Quantifying Internal Electric Fields in Organic Bulk Heterojunctions

by

Joshua Daniel Morris, B.S.

Dissertation

Presented to the Faculty of the Graduate School of

The University of Texas at Austin

in Partial Fulfillment

of the Requirements

for the Degree of

Doctor of Philosophy

The University of Texas at Austin

May 2013

Dedication

For Lillian

Acknowledgements

There are many individuals who have made this dissertation, and my development as a scientist, possible. I would like thank my advisor, Xiaoyang Zhu, for his enthusiasm and encouragement. Through his continual motivation I have grown as an experimentalist and as a physical chemist. I would also like to thank Loren Kaake, Raluca Gearba, and Heungman Park for their willingness to engage in long discussion and for their crucial suggestions throughout my time in graduate school. I would like to thank Adam Garland for thoughtfully listening and providing feedback on the current state of my projects on nearly a daily basis. Additionally I would like thank John Tritsch for helping me with a myriad of technical problems. I would also like to thank Tim Atallah for his hard work and valuable contributions to all of the microcopy experiments in this thesis. Further I would like to express my gratitude to Wai-Lun Chan, Luis Miaja-Avila, Kenrick Williams, Cory Nelson and Andrei Dolocan for helping me to troubleshoot whenever a problem arose with my optical setup. I would like to thank Nick Monahan for insightful and passionate discussions on a wide variety of topics. I would also like to thank the entire Zhu group for providing a strong environment for scientific development. Finally I would like to thank Katherine Willets and the Willets Group for providing feedback on my research and supporting me through the process of writing this dissertation.

Quantifying Internal Electric Fields in Organic Bulk Heterojunctions

Joshua Daniel Morris, Ph. D.

The University of Texas at Austin, 2013

Co-Supervisor: Katherine Willets

Co-Supervisor: Xiaoyang Zhu

Renewable forms of energy are becoming increasingly important as the world quickly depletes its current energy reserves, and rapidly increases the concentration of pollutants in our environment. Solar technology based on organic semiconductors provides a promising candidate to fulfill a portion of our future energy needs in an environmentally sustainable manner. Organic semiconductors are a collection of pi-conjugated small molecules and polymers which can be implemented in photovoltaic cells that are potentially quite low cost. Currently, however, their commercial applications are limited due to a relatively low efficiency in converting sunlight into usable power. The fundamental physics of such devices must be clarified if these materials are to compete with traditional inorganic solar cells.

In this dissertation, two emerging experimental tools are implemented in investigations of the internal electric fields present within operating organic photovoltaic cells. The first set of investigations utilizes the vibrational Stark effect to quantify the electric fields which often form at the interfaces between two organic semiconducting

materials. Such interfaces are at the heart of the photocurrent generation process in these devices and any electric fields formed crucially alter device performance. We quantitatively determine the interfacial field present in blends of poly(3-hexylthiophene) (P3HT) and phenyl-C61-butyric acid methyl ester (PCBM) and show that this field depends strongly on annealing conditions. Finally we discuss a correlation between this interfacial electric field, crystalinity and device performance.

The second set of investigations take advantage of electric field induced second harmonic generation microscopy to examine the electric potential across active organic solar cells. We again investigate blends of PCBM and P3HT as well as poly(4,4-dioctyldithieno(3,2-b:2',3'-d)silole)-2,6-diyl-alt-(2,1,3-benzothiadiazole)-4,7-diyl) (PSBTBT) and PCBM. In the former we find that the potential drop across the device shifts dramatically over time under illumination, while in the latter we find a nearly linear drop which remains constant through device operation. We then extend our examinations of PSBTBT:PCBM with EFISH by quantifying the extent of space charge accumulation throughout such devices.

Table of Contents

List of Tables

List of Figures

Chapter 1: *Introduction*

1.1 MOTIVATION

Renewable forms of energy are becoming increasingly important as the world quickly depletes its current energy reserves, and rapidly increases the concentration of pollutants in our environment. Solar technology provides a promising candidate to fulfill a portion of our future energy needs in an environmentally sustainable manner. Currently the market prices of such technology prevents its wide spread adoption. Without significant shifts in the regulatory environment, the only path to increase solar technology's prevalence is through reducing cost. This can be accomplished by increasing efficiency or by lowering manufacturing costs (1).

One promising candidate, with potentially quite low manufacturing cost, are photovoltaic cells comprised of organic semiconductors. Organic semiconductors are a class of pi-conjugated small molecules and polymers which were first investigated in the 1950s after high conductivities were reported in perylene-bromine complexes (2). They were first implemented in a solar cell in 1986 when Ching Tang, a scientist working at Kodak, made the first heterojunction organic solar cell (3).

Many of these molecular semiconductors are solution processable allowing them to be printed in a roll-to-roll fashion much like newspapers. Additionally they can be used in wide-ranging applications besides photovoltaic cells, including light emitting diodes and field effect transistors (4).

Currently, however, the efficiency of these organic solar cells are below values

which make them cost competitive with traditional photovoltaic cells (5). In recent years, there has been substantial improvement with the record photovoltaic efficiency for organic devices jumping from just 5% to above 10% in just five years (6). Despite this progress and increased interest in these materials, there are still many open questions in the field which hinder further progress such as: How do electron-hole pairs efficiently separate? What is the origin of the electric field at the interface between two organic semiconductors? How do these devices change during the course of operation? How does charge carrier mobility depend on the composition of these photovoltaic cells? This thesis addresses several of these questions through the development of techniques to characterize this emerging class of semiconductors.

1.2 ORGANIZATION OF THESIS

In this thesis, two emerging experimental tools will be examined which aid in our understanding of organic semiconductors. The first tool implements the vibrational Stark effect, in combination with attenuated total reflection Fourier transform infrared spectroscopy, to investigate the interfacial electric fields which often occur when two organic semiconductors are brought into contact. The second tool introduced is electric field induced second harmonic generation (EFISH) microscopy, which is utilized to map the potential drop across active organic photovoltaic cells. In order to appreciate the questions which these techniques address, some relevant background knowledge is required. For this reason, chapter 2 introduces organic semiconductors and discusses some crucial differences between these materials and traditional inorganic

semiconductors. After laying some basic foundations, chapter 2 continues by discussing two key challenges in the top performing organic solar cells which are addressed experimentally in later chapters.

In chapter 3, the experimental background of EFISH is developed in detail. This discussion begins with an analysis of some basic results of nonlinear optics and then extends this understanding to include electric field induced second harmonic generation. Finally we examine the details of our microscopy technique which allow us to quantitatively map electric fields in active solar cells.

In chapter 4, we implement the vibrational Stark Effect to investigate blends of organic semiconductors. This technique allows us to quantitatively determine the magnitude of the electric field which forms at the interface between two organic semiconductors under a variety of annealing conditions. We also detail the impact of solvent (which is sometimes present within these blends) on such measurements, and we introduce a method to quantitatively determine the portion of these films which are crystalline (which we corroborate with grazing incidence x-ray diffraction). Finally we discuss a correlation between this interfacial electric field, crystalinity and device performance.

In chapter 5, we map the electric field in two devices comprised of two organic blends with EFISH microscopy. The first blend, poly(3-hexylthiophene) (P3HT) and phenyl-C61-butyric acid methyl ester (PCBM), has been broadly investigated in the past. While the second blend, poly(4,4-dioctyldithieno(3,2-b:2',3'-d)silole)-2,6-diyl-alt-(2,1,3-benzothiadiazole)-4,7-diyl) (PSBTBT) and PCBM, incorporates a cutting edge polymer which comes from an

emerging class of low band gap organic semiconductors. In the former we find that the potential drop across the device shifts dramatically over time under illumination, in the latter we find a nearly linear drop which remains constant through device operation. We conclude by discussing what these potential maps imply about the electron and hole mobility in each blend.

In chapter 6, we extend our examinations of PSBTBT:PCBM with EFISH microscopy by varying the relative proportion of each semiconductor within an active organic devices. We observe that the potential drop shifts dramatically based on composition, and conclude that shifts in electron and hole mobility based on composition are primarily responsible for such changes. Finally we quantify the extent of space charge accumulation throughout each of our devices.

Chapter 2: *Organic Solar Cells: Background and Challenges*

2.1 ORGANIC SEMICONDUCTORS

Organic semiconductors are an emerging class of materials comprised of pi-conjugated small molecules and polymers. As discussed in the introduction, these materials are potentially quite low cost and have applications in photovoltaic cells, organic light emitting diodes, and field effect transistors. If these devices are to become cost competitive with traditional inorganic semiconducting devices, a more thorough understanding of their properties must be attained (7). When studying these systems, it is tempting to import the theoretical background which underpins inorganic semiconductors without a critical examination of the wide array of differences between the two materials (8). What follows is a discussion of the several relevant properties of organic semiconductors which highlight these differences.

2.1.1 Charge Transport in Organic Semiconductors

One key difference between inorganic semiconductors and their organic counterparts is the nature of charge transport within these materials. In doped silicon or germanium, conduction proceeds through band transport which is well described by the Drude model (9). The Drude model uses kinetic theory to describe conductivity as a competition between two processes: the constant acceleration of charge carriers due to an applied electric field, and the frequent collisions between carriers and the ionic cores of the lattice through which these carriers are moving. This gives rise to a linear relationship

between the applied field and current density. For a semiconductor with negligible conductivity from holes we have (10),

$$\mathbf{J} = \left(\frac{nq^2\tau}{m^*} \right)\mathbf{E}, \tag{2.1}$$

where ***J*** is the current density, n is the free carrier density, q is the charge of the carrier, τ is the mean time scale between collisions with the ionic cores, m^* is the effective mass of the charge carrier, and ***E*** is the electric field. If significant conductivity arises from holes, then a similar term must be added for this contribution, but the underlying principles remain the same. It should be noted that while equation 2.1 has no explicit temperature dependence (or dopant concentration dependence), any changes in temperature (or dopant concentration) will directly affect the number of free carriers available and hence conductivity. The important message is that we can effectively model conductivity in inorganic semiconductors by considering the paths of the charge carriers through a field of fixed ionic cores as shown Fig. 2.1.

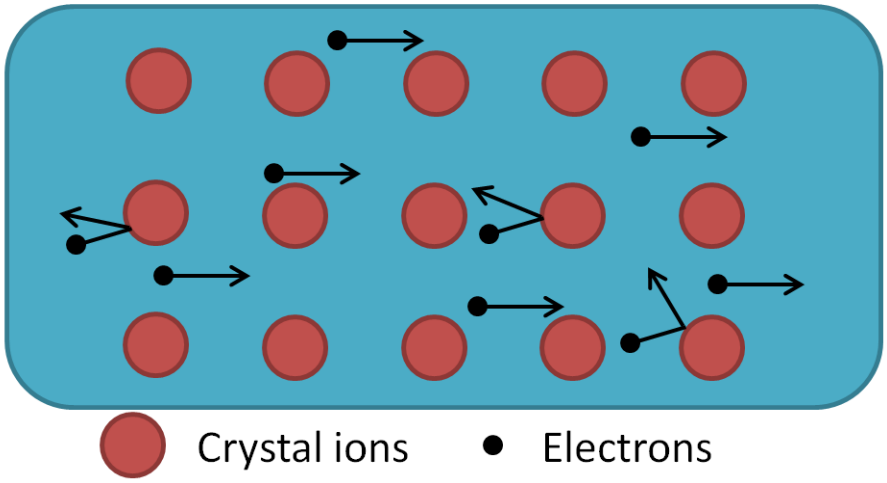

Figure 2.1: Schematic of the Drude model showing the conducting electrons (black) as they are accelerated by an electric field through the fixed ionic cores (red) of a crystal lattice.

This simple picture of charge transport in inorganic semiconductors completely neglects shifts in nuclear coordinates due to the presence of charge carriers. While this approximation is quite justified in the case of traditional semiconductors, it is unlikely to be acceptable in organic materials where strong electron-phonon coupling is the norm (11). This coupling leads to nuclear reorganization that crucially affects charge transport. A detailed description of the models of charge transport in these materials is beyond the scope of this thesis. However, several general points should suffice to clarify conduction in organic semiconductors for our purposes.

In most cases, the dominant charge transport mechanism in organics is thermally activated hopping, which is well described by Marcus Theory (11). This model was originally developed in the 1950's by the Nobel laureate, Rudolph Marcus, to describe electron transfer rates between chemical species in an aqueous environment (12). Under

this picture, the rate of electron transfer between a donor and acceptor depends strongly on structural reorganization which takes place when a species undergoes a change in oxidation state. The rate of electron transfer from a given donor to a given acceptor in its most general form is given by (13),

$$k_{et} = A\exp\left(\frac{-(\lambda + \Delta G^{\circ})^2}{4\lambda k_b T}\right), \qquad (2.2)$$

where A is a prefactor which depends on the type of electron transfer, k_{et} is the rate of electron transfer, λ is the reorganization energy, k_b is the Boltzmann constant, T is temperature, and finally, $\Delta G°$ is the change in Gibbs free energy. The applicability of a model originally developed for isolated electron transfer reactions between two localized sites to organic semiconductors highlights two important features of charge transport these systems. Firstly, charges in organic semiconductors tend to localize around a specific molecular site and secondly, charge transport proceeds in a stepwise fashion between these localized sites. This contrasts with the Drude model where an electron is delocalized within a band.

In should be noted that in particularly well ordered organic systems, such as single crystal ruberene, charge transport can be well described by the Drude model (14). This is particularly the case at low temperatures where contributions from thermally activated hopping are minimized. The important point, however, is that modeling charge transport through organic semiconductors requires careful considerations of how carriers

rearrange their environment, while in inorganic materials this interaction can typically be neglected.

2.1.2 Photo-exciation in Organic Semiconductors

Another relevant difference between inorganic and organic semiconductors is the nature of photo-excited electron-hole pairs in these systems. When light impinges on these pi-conjugated materials, an electron is excited from the highest occupied molecular orbital (HOMO) to the lowest unoccupied molecular orbital level (LUMO). This electron leaves behind a vacancy known as a hole. This electron-hole pair, schematically shown in Fig. 2.2, known as an exciton, remains columbically bound due to the relatively low dielectric constant of organic materials. This binding energy is on the order of a few hundred meV, well in excess of the available thermal energy at room temperature (15). This contrasts with similar excitations in inorganic semiconductors which give rise to excitons with a binding energy on the order of thermal energy (in this case due to the relatively high dielectric constant).

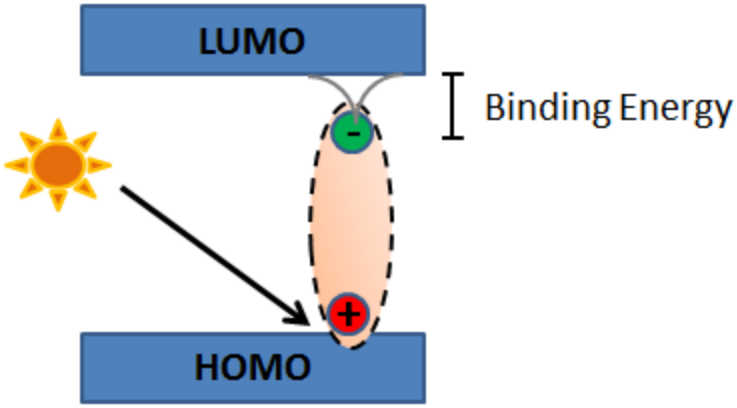

Figure 2.2: Schematic of a photo-excitation in an organic semiconductor showing the binding energy between the electron and hole.

2.2 PLANAR HETEROJUNCTION SOLAR CELLS

The generation of photocurrent in organic solar cells requires the effective splitting of these tightly bound excitons. Such splitting is unlikely in the bulk of a single organic compound. For this reason, effective organic solar cells are typically comprised of two organic semiconductors, an electron donor and an electron acceptor. The offset between the LUMO of the electron donor and the LUMO of the electron acceptor (shown in Fig. 2.3a) provide a portion of the necessary driving force to separate photogenerated excitons in these systems (16). The simplest combination of an electron donor and acceptor involves a single layer of the electron and donor and a single layer of the electron acceptor sandwiched between two electrodes as shown in Fig. 2.3b.

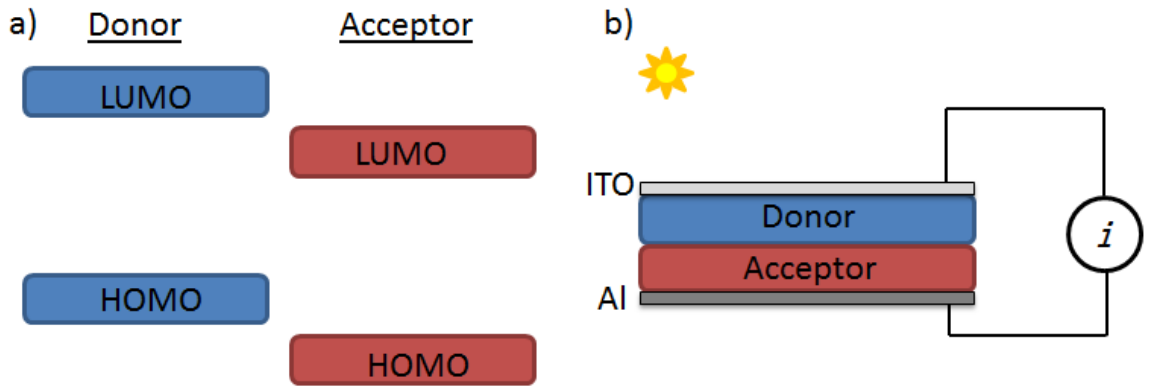

Figure 2.3: a) The binding energy between the electron hole gives rise to difference between the conduction level for isolated electrons and the optical absorption maximum. b) A schematic of a planar bulk heterojunction. The top electrode must be transparent and is generally indium tin oxide (ITO).

In order to generate photocurrent an exciton generated in the acceptor or donor must diffuse to the donor/acceptor interface where it can then separate into two free carriers. After this separation the charges then migrate back to the appropriate electrode for collection. This charge migration is driven by a built in field which is due to a difference in work function between the cathode and anode (17). These steps of photogeneration are shown in Fig. 2.4.

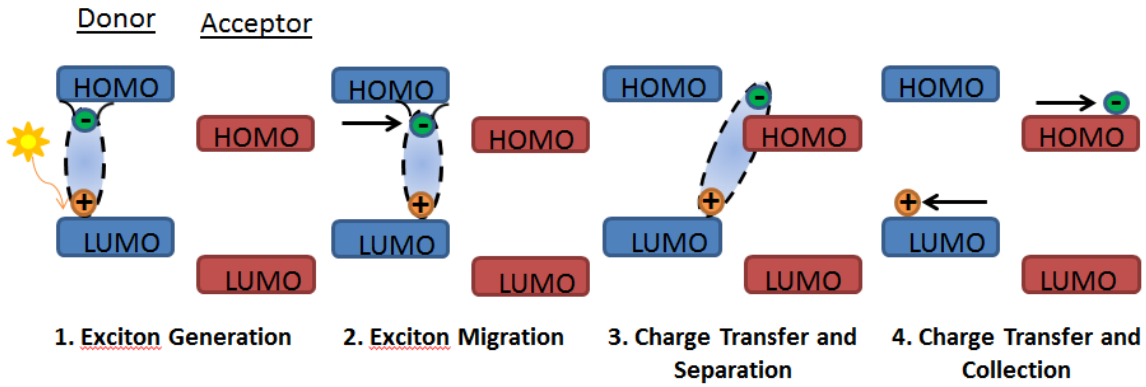

Figure 2.4: The crucial steps in photocurrent generation in organic photovoltaic cells.

Recently the importance of the exciton migration step shown in Fig. 2.4 has been called into question. It seems that majority of photocurrent arises from excitons generated immediately at the interface between the electron and donor (18-19). For this reason it is crucially important to maximize the donor/acceptor interface to allow for maximum photocurrent generation. While the planar heterojunction is a simple model to understand the photogeneration process it turns out that they typically have quite low efficiencies (20).

2.3 BULK HETEROJUNCTION SOLAR CELLS

Bulk heterojunctions (BHJs) considerably increase the donor/acceptor interface by spincoating a mixture of the electron donor and acceptor from a single solution. This leads to a film with interpenetrating domains of donor and acceptor as shown in Fig. 2.5 (21). In addition to increasing the donor/acceptor interface, these domains typically allow for effective charge migration of separated electrons and holes back to the appropriate electrode.

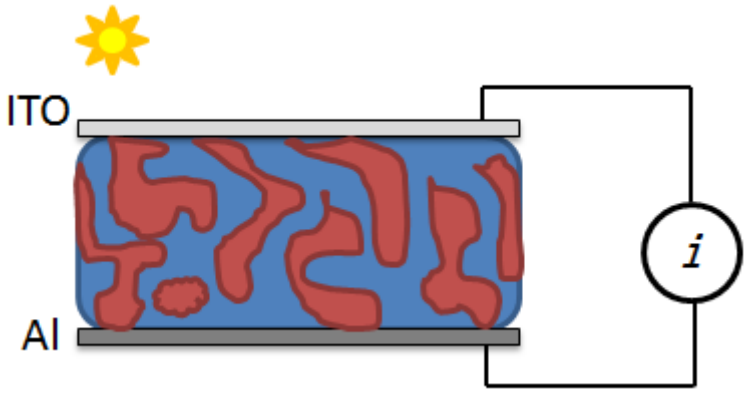

Figure 2.5: A schematic of an organic bulk heterojunction. This device geometry considerably increases the donor/acceptor interface when compared to planar heterojunctions.

The top performing organic photovoltaic cells are typically comprised of BHJ films (22). These systems are intricate solids comprised of crystalline and amorphous regions which can be tuned through thermal and solvent annealing. This complex morphology complicates theoretical descriptions of these devices as small differences in morphology and crystallinity can result in considerably different device physics (23).

2.4 Challenges in Organic Photovoltaic Cells

This section will examine two challenges in organic photovoltaic systems which are particularly relevant to the experimental investigations discussed in this thesis.

2.4.1 Interfacial Electric Fields

When two organic semiconductors are brought into contact (for example at the donor/acceptor interface) an electric field can be generated. The mechanistic origins of this field are still a matter of dispute, though ultimately, it must arise from charge carrier redistribution either through charge transfer or polarization effects (24-25). It should be pointed out that due to the diverse array of molecular systems which comprised organic devices, it may be possible that the mechanism giving rise to such a field could vary from interface to interface.

This electric field critically affects organic photovoltaic devices, as a field formed at the donor/acceptor interface will shift the molecular orbital levels of each system. These molecular orbital levels, and their relative alignment, determine the absorption maximum of each species and critically alter the efficiency of exiton splitting (26).

These changes in molecular orbital levels also complicate targeted design of new organic semiconductors by chemists. Ideally, we could modify organic semiconductors to have the appropriate band gap for optimal solar absorption and the ideal relative alignment between donor and acceptor to maximize the efficiency of exciton splitting. However, when the isolated molecular orbitals differ from those energetic levels in an actual device this process becomes significantly more difficult (27). The optimal solution to this problem would involve a mechanistic understanding of this interfacial electric field which allows these shifts to be predicted. Barring this, however, it would be an important step to develop a quick method to determine the interfacial electric field in

donor/acceptor systems which could then inform further modifications of these organic semiconductors.

2.4.1 Space Charge Accumulation

In the process of generating photocurrent, both electrons and holes are extracted from an active device. Frequently it is the case that each charge carrier has a different characteristic drift length. An electron's drift length is given by (28),

$$L = \mu_n \tau_n E, \tag{2.3}$$

Where μ_n is the electron mobility, τ_n is a phenomenological parameter which includes the timescale until recombination or charge trapping, and E is the local electric field. The expression for holes is obtained simply by substituting the appropriate mobility and timescale. Since the timescale is generally assumed to be similar for both electrons and holes, the primary reason for two carriers to have a different drift length is the result of different mobilities. If these mobilities differ significantly, then upon initial illumination of an organic device the fast carrier will be collected at a higher rate. For example, if $\mu_h >> \mu_e$, then, transiently, more holes than electrons would be collected, leading to an accumulation of electrons within each device, as shown in Fig.2.6b. These holes will disproportionately accumulate at the negatively biased electrode; eventually this accumulation balances charge collection of electrons and holes by changing E in Eq.2.3 in the vicinity of electron/hole collection as shown in Fig. 2.6d.

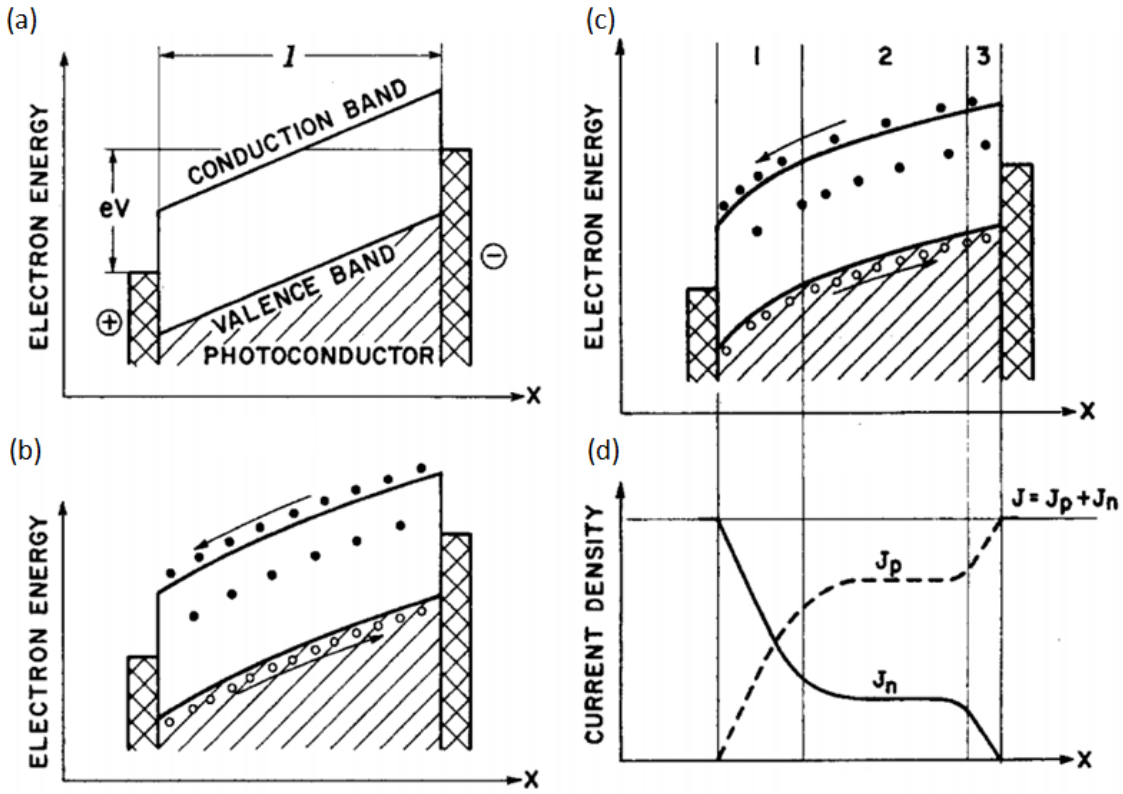

Fig.2.6 a) A schematic of a semiconductor from which both holes and electrons can be simultaneously extracted. b) Initial charge collection before equilibrium is reached, electrons are accumulating in the device since the hole mobility is higher than the electron mobility. c) The device at equilibrium, after the local potential has been deformed due to charge accumulation. d) a schematic showing both electron and hole conduction as a function of position. Such a device can be thought of in terms of the three regions in part c and d. In region 1 and 3 net photocurrent is generated, and in 2 photocurrent generation equals recombination. Reprinted with permission from A. M. Goodman, A. Rose, "Double Extraction of Uniformly Generated Electron-Hole Pairs from Insulators with Noninjecting Contacts," *J. Appl. Phys*. **42**, 7, 1971. © 1971 American Institute of Physics.

Under such circumstances, we can view a device as comprised of three regions as shown in Fig.2.6c and d. In region one, we have the net accumulation of electrons adjacent to the electron collecting electrode. In region three, we similarly have a net

accumulation of holes adjacent to the hole collecting electrode. The spatial extent of these regions is given by (28),

$$l_i = \sqrt{\mu_j \tau_j V_i}, \tag{2.4}$$

where l_i is the length of either region 1 or 3, μ_j and τ_j is the mobility and the timescale of recombination respectively, for holes in the case of region 1, and for electrons in the case of region 3. Finally, V_i is the voltage in the appropriate region. If the device length, L, is larger than $l_1 + l_3$ then we have an additional region in the device center which maintains charge neutrality. Charge carriers generated in this region are not collected, since the distance to the electrodes is greater than their drift lengths. This implies that all net current generation arises from region one and three while in region two charge carrier generation and recombination are equal.

The buildup of charge carriers in region one and three is known as space charge accumulation and it imposes a fundamental electrostatic limit on the maximum amount of current which be extracted from a device. This phenomenon was first brought to light in theoretical work by Goodman and Rose in the 1970s. In their analysis, they show that a space charge limited device's photocurrent is given by (29),

$$J_{scl} = q\left(\frac{9\varepsilon_0 \varepsilon_r \mu_s}{8q}\right)^{1/4} G^{3/4} V^{1/2}, \tag{2.5}$$

where q is the electric charge, ε_0 is the permittivity of free space, ε_r is the dielectric constant, μ_s is the mobility of the slow carrier, G is the generation rate, and V is the applied voltage. In contrast photocurrent from such devices typically is given by (29),

$$J_{ph} = qG(\mu_s \tau_s V)^{1/2}, \quad (2.6)$$

In the former case the photocurrent depends on $G^{3/4}$, while in the latter it depends directly on G. In addition to imposing a fundamental limit on the extraction of photocurrent, space charge accumulation also increases charge carrier recombination and results in lower fill factors and hence lower efficiencies. Previously space charge accumulation has primarily been studied indirectly through current-voltage measurements when the photocurrent is determined to be dependent on $G^{3/4}$ (29). Unfortunately, a variety of factors can shift a photovoltaic cell's dependence on the generation rate (30). If space charge accumulation is to be investigated rigorously, new experimental techniques are required.

Chapter 3: *Electric Field Induced Second Harmonic Generation Microscopy*

In this chapter the foundations of EFISH microscopy will be laid out in order to fully understand the experimental basis for experimental results discussed in chapter 5 and 6.

3.1 NONLINEAR OPTICS AND WAVE MIXING PHENOMENA

Typically the polarization induced in a material by an electric field is approximated by (31),

$$P(t) = \varepsilon_0 \chi^{(1)} E(t), \tag{3.1}$$

where P(t) is the time varying induced polarization, ε_0 is the permittivity of free space, $\chi^{(1)}$ is the linear susceptibility, and E(t) is the time varying electric field. This simple linear relationship provides effective estimates of the induced polarization in materials under most circumstances. It turns out, however, that the relationship between an induced polarization and an applied electric field is considerably more complex. It can be expressed as a power series in the field strength E (31),

$$P(t) = \varepsilon_0 \left[\chi^{(1)} E(t) + \chi^{(2)} E(t)^2 \chi^{(3)} E(t)^3 + \ldots \right], \tag{3.2}$$

where χ^n is the nth order susceptibility term. Immediately it is apparent from Eq. 3.2 that an induced polarization depends nonlinearly on an applied electric field. However, since χ^{n+1} is typically orders of magnitude smaller than the previous term χ^n, the higher order terms can typically be neglected (there are, of course, many special cases where this is

not true) (32). However, at sufficiently high electric field strengths (such as those present in the optical field of a laser), higher order terms often contribute significantly.

These terms which depend nonlinearly on the applied electric field strength can give rise to a range of new phenomena which are observed when high enough light intensities are present. For example, if we consider the second order polarization,

$$P^{(2)}(t) = \varepsilon_0 \chi^{(2)} E(t)^2, \tag{3.3}$$

and a field of the form,

$$E(t) = E_1 e^{-i\omega_1 t} + E_2 e^{-i\omega_2 t} + c.c., \tag{3.4}$$

where $P^{(2)}$ is the second order polarization, E_n and ω_n are the nth electric field strength and the corresponding phase, and c.c. is the corresponding complex conjugate, we find that (33):

$$P^{(2)}(t) = \varepsilon_0 \chi^{(2)} \left| E_1 e^{-i\omega_1 t} + E_2 e^{-i\omega_2 t} + c.c. \right|^2,$$

$$= \varepsilon_0 \chi^{(2)} \left[E_1^2 e^{-2i\omega_1 t} + E_2^2 e^{-2i\omega_2 t} + 2E_1 E_2 e^{-i(\omega_1+\omega_2)t} + 2E_1 E_2^* e^{-i(\omega_1-\omega_2)t} + c.c. \right]$$

$$+ 2\varepsilon_0 \chi^{(2)} \left[E_1 E_1^* + E_2 E_2^* \right] \tag{3.5}$$

From just the second order polarization term we can observe a number of unique phenomena. Each term within the brackets gives rise to a new optical wave with a new frequency. We can see that a terms with the following frequencies: $2\omega_1$, $2\omega_2$, $\omega_1+\omega_2$, and finally $\omega_1-\omega_2$. The generation of these new optical waves at $2\omega_1$ or $2\omega_2$ is known as second harmonic generation (SHG). The practical implication of SHG is that a sufficiently intense beam of photons at ω passing through a nonlinear optical medium will

generate a beam of photons at 2ω. Generating an optical wave at $\omega_{1+}\omega_2$ is known as sum frequency generation (SFG), which allows us to use a nonlinear medium to generate a new optical wave at $\omega_1+\omega_2$ from two separate incident waves at ω_1 and ω_2. Finally generating a wave at $\omega_1-\omega_2$ is called difference frequency generation (DFG). Fig. 3.1 summarizes all of the process which can arise from the second order polarization incident on a nonlinear medium.

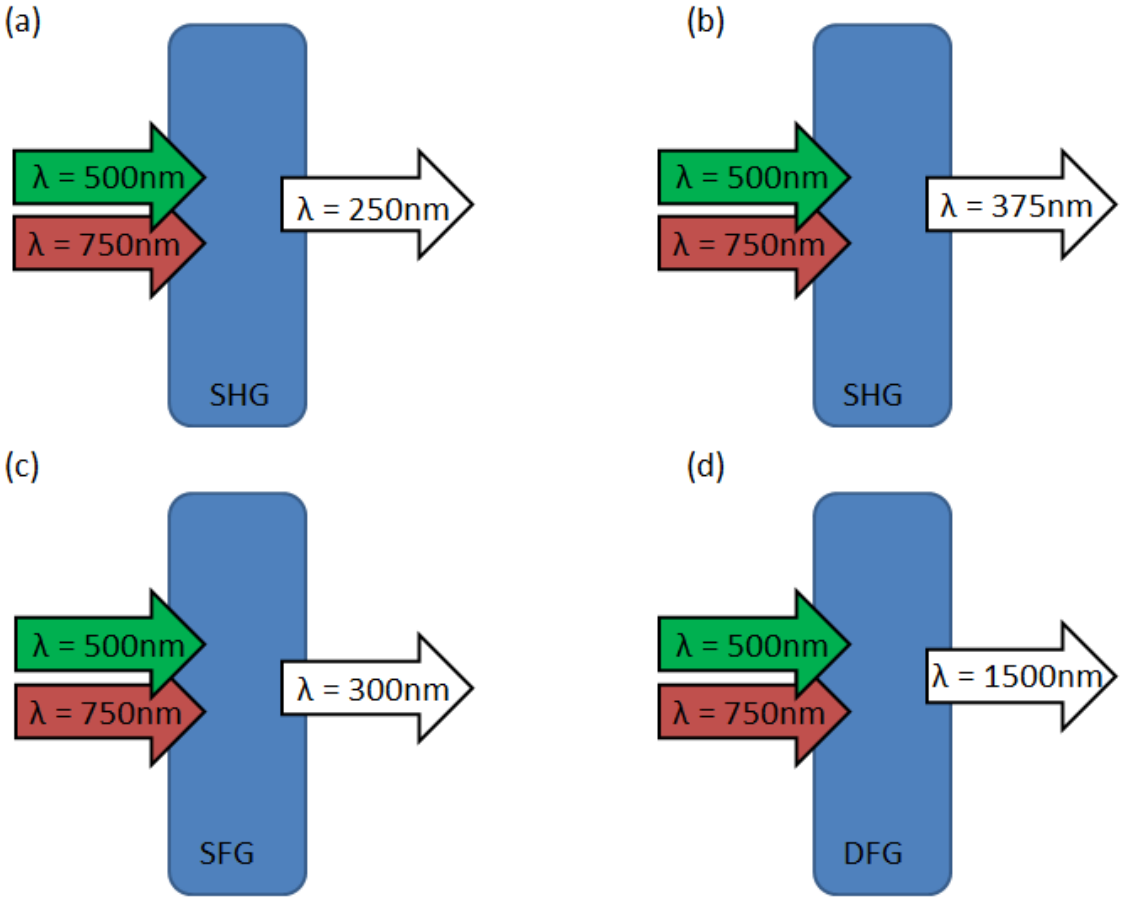

Figure 3.1: a) Second harmonic generation arising from the 500 nm light. b) Second harmonic generation arising from the 750 nm light. c) Sum frequency generation arising from both the 500 nm and 750 nm light. d) Difference frequency generation arising from both the 500 nm and 750 nm light. Obviously, all four of these processes are occurring simultaneously and hence light at six distinct frequencies will exit this material. Two from the incident beams and four generated through nonlinear optical processes.

3.2 Electric Field Induced Second Harmonic Generation

EFISH is a special case of second harmonic generation where the conversion of two incident photons of frequency ω to a single photon of frequency 2ω depends on the

strength of a DC electric field present within a system (34). The total second harmonic signal in the presence of an electric field is given by (35),

$$\begin{aligned} I^{2\omega} &= \left| E_0^{2\omega} e^{i\varphi_0} + E_{EFISH}^{2\omega} e^{i\varphi_{EFISH}} \right|^2 \\ &= \left(E_0^{2\omega}\right)^2 + \left(E_{EFISH}^{2\omega}\right)^2 + 2E_0^{2\omega} E_0^{2\omega} \cos(\varphi_0 - \varphi_{EFISH}), \end{aligned} \tag{3.6}$$

where $E_0^{2\omega}$ and φ_0 are the second harmonic field and the corresponding phase in the absence of any EFISH contributions, $E_{EFISH}^{2\omega}$ and φ_{EFISH} are the second harmonic field and the corresponding phase arising from the DC electric field, and $I^{2\omega}$ is the total second harmonic intensity. The last term in Eq. 3.6 can pose significant problems when analyzing second harmonic intensity as the phase difference $\cos(\varphi_0 - \varphi_{EFISH})$ is typically unknown. This is particularly problematic when quantifying the intensity as a function of position across a sample, as subtle differences in sample thickness or morphology can change this phase relationship considerably.

3.3 EFISH Microscopy of Organic Bulk Heterojunctions

Fortunately the EFISH investigations in this thesis examine organic bulk heterojunctions which are centrosymmetric. In this case, under the dipole approximation, contributions from $E_0^{2\omega}$ in Eq. 3.6 can be neglected (assuming surface contributions are also negligible). In this case the total second harmonic intensity can be reduced to (36)

$$I^{2\omega} = \gamma \left| E_{EFISH}^{2\omega} \right|^2 = \gamma \left| \chi_{ijkl}^{(3)} E^{\omega} E^{\omega} E^{DC} \right|^2 = \gamma \left| \chi_{eff}^{(3)} \right|^2 \left(I^{\omega}\right)^2 \left(E^{DC}\right)^2, \tag{3.7}$$

where γ is a constant which depends on the sample geometry and includes the appropriate Fresnel factors, $\chi^{(3)}_{ijkl}$ is the third order nonlinear susceptibility, $\chi^{(3)}_{efl}$ is the effective third order nonlinear susceptibility and E^{DC} time constant electric field present within a system. In this case, the phase dependence can conveniently be neglected.

In order to effectively interpret second harmonic intensity, we need to understand how E^{DC} is mapped to our intensity, $I^{2\omega}$, by $\chi^{(3)}_{ijkl}$. In general a fourth rank tensor will have 81 individual elements. However, for centrosymmetric materials only seven nonzero terms remain. The total second harmonic polarization at 2ω in each direction (defined in Fig. 3.2) is given by (37),

$$P_x^{2\omega}(2\omega) = \chi^{(3)}_{xxxx} E_x(\omega) E_x(\omega) E_x^{DC}(0) + \chi^{(3)}_{xyyx} E_y(\omega) E_y(\omega) E_x^{DC}(0), \tag{3.8}$$

$$P_y^{2\omega}(2\omega) = \chi^{(3)}_{yyyy} E_y(\omega) E_y(\omega) E_y^{DC}(0) + \chi^{(3)}_{yxxy} E_x(\omega) E_x(\omega) E_y^{DC}(0), \tag{3.9}$$

$$\begin{aligned} P_z^{2\omega}(2\omega) &= \chi^{(3)}_{zzzz} E_z(\omega) E_z(\omega) E_z^{DC}(0) + \chi^{(3)}_{zyyz} E_y(\omega) E_y(\omega) E_z^{DC}(0) \\ &+ \chi^{(3)}_{zxxz} E_x(\omega) E_x(\omega) E_z^{DC}(0), \end{aligned} \tag{3.10}$$

where $\chi^{(3)}_{ijkl}$ is a specific tensor element, $E_i(\omega)$ is the incident field at frequency ω with i polarization, and where E_i^{DC} is the electric field in the i direction within the material of interest.

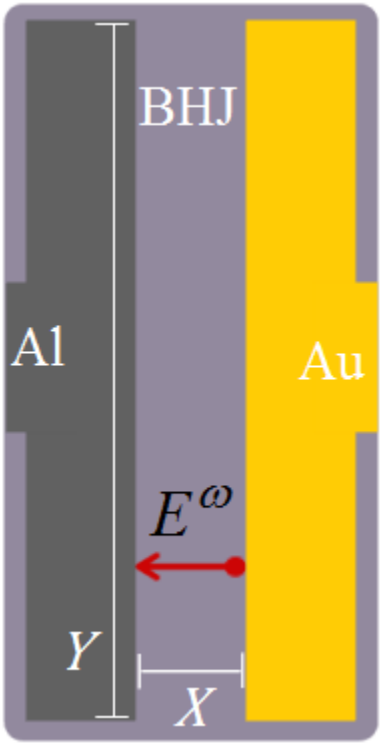

Figure 3.2: A schematic of the sample geometry used in the EFISH microscopy experiments. The red line represents the polarization of the incident electric field (in this case in the x direction). The y dimension is on the order of 20 microns and the x dimension typically spans one millimeter. The positive z direction in this case is coming out of the page.

Conveniently if the incident electric field $E_i(\omega)$ is strongly polarized in the x-direction we can reduce Eq.3.8 to 3.10 to,

$$P_x^{2\omega}(2\omega) = \chi^{(3)}_{xxxx} E_x(\omega) E_x(\omega) E_x^{DC}(0), \tag{3.11}$$

$$P_y^{2\omega}(2\omega) = \chi^{(3)}_{yxxy} E_x(\omega) E_x(\omega) E_y^{DC}(0), \tag{3.12}$$

$$P_z^{2\omega}(2\omega) = \chi^{(3)}_{zxxz} E_x(\omega) E_x(\omega) E_z^{DC}(0). \tag{3.13}$$

Further we can neglect any contributions from Eq. 3.13, as any optical fields with z-polarization will propagate in a direction perpendicular to the incident beam and will not

be detected. From equations 3.11 and 3.12 we can see that by selecting the correct polarization we can easily map both E_x^{DC} and E_y^{DC} separately. When we observe the x-polarized light our second harmonic intensity will be given by:

$$I^{2\omega} \approx \gamma \left| \chi^{(3)}_{xxxx} \right|^2 \left(I^{\omega} \right)^2 \left(E_x^{DC} \right)^2, \tag{3.14}$$

and by selecting the y-polarized light our second harmonic intensity will be given by:

$$I^{2\omega} \approx \gamma \left| \chi^{(3)}_{yxxy} \right|^2 \left(I^{\omega} \right)^2 \left(E_y^{DC} \right)^2, \tag{3.15}$$

though in the samples investigated in this thesis it is always observed that $E_x^{DC} >> E_y^{DC}$.

3.4 Experimental Implementation of EFISH Microscopy

3.4.1 Optical Layout and Data Acquisition

All EFISH microscopy images in this thesis were taken in transmission mode with a fundamental beam at 1060 nm (~200 fs, 76 MHz, pulse energy ~ 2 nJ) generated by an optical parametric oscillator (Coherent Mira-OPO) pumped by a Ti:sapphire oscillator (Coherent Mira HP), Fig. 3.3. The 1060 nm laser beam was focused by an f = 10 cm lens to a diameter of 80 μm on the device surface which is on a transparent substrate. The second harmonic signal at 530 nm was imaged by a microscope objective (Mitutoyo 20X) and recorded on an EM-CCD camera (Andor Technology 897E) which was cooled to 170 K thermoelectrically. Using appropriate bandpass and/or cutoff filters, we obtained images either at 1060 nm (fundamental) or 530 nm (EFISH).

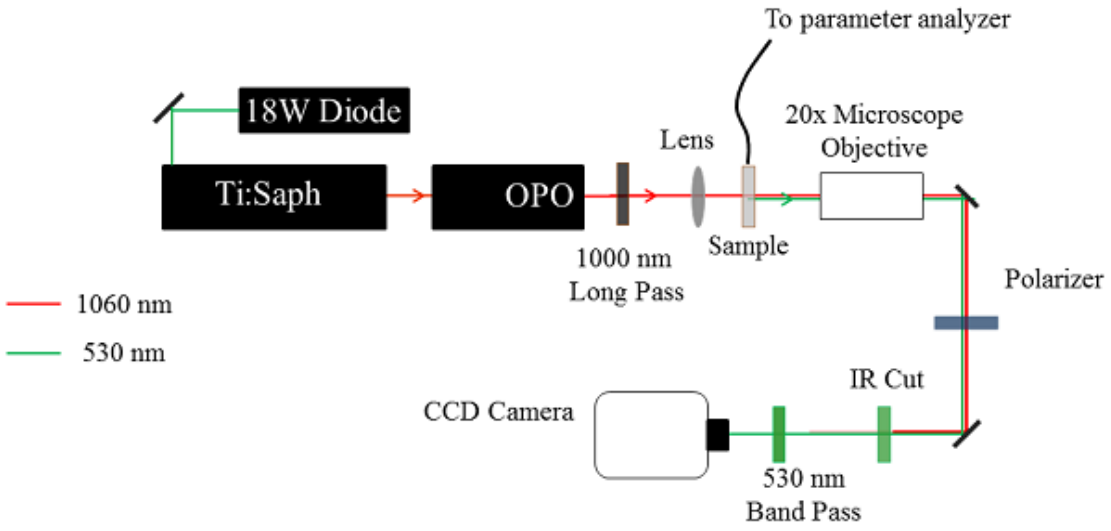

Figure 3.3: The optical layout used in our EFISH microscopy experiments. Pulsed IR light generated by the optical parametric oscillator is passed through a 1000 nm long pass to remove any trace second harmonic light, and is then focused onto our organic bulk heterojunction sample where the EFISH signal is generated. This light is collected by the microscope objective and the filtered appropriately before being collected by our EM-CCD.

In order to collect an EFISH image a constant voltage of 200V is applied to our organic bulk heterojunction samples while the second harmonic intensity is integrated over a period of 30 to 60 seconds.

3.4.2 Generating Quantitative Electric Field Maps from EFISH Microscopy

In section 3.3 it was shown that, under certain assumptions (namely the dipole approximation and minimal surface contributions), that our second harmonic signal was proportional to the square of the electric field present within our system (as seen in Eq. 3.14 and 3.15). The electric fields observed in our organic bulk heterojunction

systems arise from a known applied potential, V_0, applied in the x-direction with the aluminum at a positive potential with respect to the gold. Since $E_x^{DC} \propto V_0$, we expect the average SHG intensity to be proportional to V_0^2 from Eq. 3.14. This relationship is confirmed in the log-log plot in Fig. 3.4 which plots the log of the integrated SHG intensity versus a range of applied biases, a slope of 2.0 ± 0.3 is observed. Note that if surface contributions were not negligible, or the dipole approximation was not justified, then we would expect a cross term, shown in Eq. 3.6, which depends directly on E_x^{DC} instead of $(E_x^{DC})^2$.

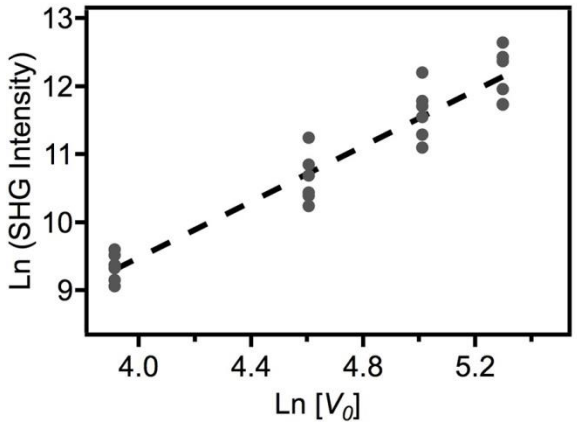

Figure 3.4: A log/log plot of integrated SHG intensities (dots) from EFISH images versus applied bias votalges. Least-square linear fit (dashed line) to the data gives a slope of 2.0 ± 0.3.

Finally, in order to quantitatively calibrate our second harmonic intensity, we start from Eq. 3.14,

$$I^{2\omega} \approx \gamma \left| \chi^{(3)}_{xxxx} \right|^2 \left(I^{\omega} \right)^2 \left(E_x^{DC} \right)^2,$$

$$I^{2\omega} \approx A^2 \left(\frac{dV}{dx} \right)^2, \tag{3.16}$$

where A is some proportionality constant. Then taking the square root of both sides and integrating we have:

$$\int_0^L \sqrt{I^{2\omega}(x)} dx = AV_0, \tag{3.17}$$

where L is the length of the channel across which V_0 is applied. So by taking the square root of our second harmonic intensity and summing this intensity across our channel length we can obtain the proportionality constant A for a particularl map of $I^{2\omega}$. Combined with equation 3.16, this allows us to quantitatively calibrate the second harmonic intensity at every point in an EFISH image to determine the electric field. Further we can then integrate this field to obtain the shape of the potential change between our two electrodes.

Chapter 4: *Quantifying Interfacial Electric Fields and Local Crystalinity in Polymer-Fullerene Bulk Heterojunction Solar Cells*

In this chapter*, we use Fourier transform infrared absorption spectroscopy to quantitatively determine the interfacial electric field in blended poly 3-hexyl-thiophene: phenyl-C61-butyric acid methyl ester (PCBM) thin films. The interfacial electric field is ~0.2 V/nm in the spin-coated film and after annealing at temperatures as high as 150 ^{o}C, which is the optimal annealing temperature in terms of OPV performance. The field decreases to a negligible value upon further annealing to 170^{o}C, at which temperature PCBM changes from amorphous to crystalline and the open circuit voltage of the solar cell decreases from 0.62 to 0.4V. In addition, our measurements also allow determination of the absolute degree of crystallinity within the acceptor material. The roles of interfacial field and local crystallinity in OPV device performance are discussed.

4.1 INTRODUCTION

Solar cells based on organic semiconductor donor/acceptor interfaces have potential to provide a cost-effective alternative photovoltaic technology for power generation (38). The highest performing organic semiconductor devices employ a bulk heterojunction architecture containing highly intermixed blends of conjugated polymer donors and

* *Much of the content of this chapter has been published as:*

R. I. Gearba, T. Mills, J. D. Morris, R. Pindak, C. T. Black, X. Y. Zhu, "Quantifying Interfacial Electric Fields and Local Crystalinity in Polymer-Fullerene Bulk Heterjunction Solar Cells", *Adv. Funct. Mater*. **21**, 2666 (2011).

fullerene acceptors (16). One of the most critical processes in organic photovoltaics is free charge generation from photogenerated excitations (39) at donor/acceptor (D/A) interfaces (40-42). Despite many studies, a complete understanding of this complex multistep process (40-42) remains elusive because of the challenges of experimentally probing the physical and electronic structure of such highly intermixed organic materials.

The power conversion efficiency (PCE) of bulk heterojunction solar cells has steadily increased in the last years and recently reached as high as 10% (6,43). These advances in solar cell performance have come largely through synthesis of new materials having modified electronic structure to optimally harvest the sunlight (materials with small band gap) and efficiently separate the excitons. The common assumption is that a few tenth of an eV difference between the lowest unoccupied molecular orbitals (LUMOs) of the donor and acceptor are enough to dissociate the excitons (44). Considering the donor and acceptor materials separately in this way neglects the significant influences of electrostatic dipoles at the heterojunction interface, which in turn depend on molecular structure, packing, orientation, charge displacement, and electronic polarization (45-48). The interfacial dipole field originates from a redistribution of electron density from the donor to the acceptor material (45-48). It may present as an energetic barrier for charge separation, but also inhibits the recombination of separated carriers (49) and can therefore alter the device photocurrent. Interfacial dipoles modify the electronic energy alignment between materials by widening the interfacial bandgap, and thus also influence the device open circuit voltage (V_{oc}) (50).

Even after successful exciton dissociation across the donor/acceptor interface, the electron-hole pair remains coulombically bound (with binding energies of a few tenths of an eV (41,52)) and therefore susceptible to interfacial recombination. The ultimate fate of such charge-transfer excitons depends critically on the local junction morphology and crystallinity (53). For example, previous models have associated the improvements in charge separation efficiency with increased delocalization of the electron and hole at interfaces resulting from changes in crystallinity and morphology upon thermal annealing (54-55). Other work has suggested that increased material crystallinity delocalizes the CT exciton wave function and thereby reduces its binding energy, explaining the high charge carrier separation efficiency by way of an increased interfacial carrier mobility (56).

Previous measurements of interfacial electric dipoles have come almost exclusively from ultraviolet photoemission spectroscopy (UPS) and reported values range from 0.1 to 1eV (57-59). UPS is a surface sensitive technique that probes only the top 1-2 nm of a film and therefore is not easily amenable to study bulk heterojunctions (53), but both structure and composition at the surface can be very different than those in the bulk (60).

In this work, we report on the use of Vibrational Stark Effect Spectroscopy (VSES) to quantitatively determine the D/A static interfacial dipole field in the complex environment of a bulk heterojunction. The vibrational Stark effect corresponds to a blue shift in the vibrational frequency of a polar bond in the presence of an external electric field (61, 62). VSES has been used successfully in the past to study the electrostatic environment in biological systems (63). A convenient reporter for this measurement is the carbonyl (-C=O) stretch vibration in phenyl-C61-butyric acid methyl ester (PCBM)

which is the classical acceptor in organic bulk heterojunction solar cells and has been used previously to monitor the time domain dynamics of charge carrier separation in polymer/PCBM heterojunctions (64-66). We correlate the magnitude of the interfacial electric field in blends processed under different conditions with the internal structure determined by grazing incidence X–ray diffraction (GIXD). We further use the difference in C=O vibrational frequency between amorphous and crystalline domains to quantify the percentage of PCBM crystallinity within the bulk heterojunction as a function of blend material processing conditions. While such spectroscopic techniques have gained acceptance in the pharmaceutical industry as a rapid and non-destructive method for determining crystallinity (67), they have not been previously used in films of semiconducting polymers or small molecules. In principle, GIXD measurements can quantitatively distinguish crystalline from amorphous regions. However, in practice this approach necessitates complex modeling (68), and measurements of a standard with known crystallinity (69). In addition, we discuss the influence of the interfacial dipoles and crystallinity on the device parameters processed under the same conditions.

4.2 RESULTS AND DISCUSSION

4.2.1 Determining the Interfacial Electric Field by the Vibrational Stark Effect

Vibrational Stark Effect Spectroscopy (VSES) provides a quantitative probe of the interfacial electric field in blends of different polymer semiconductors with PCBM (Fig. 4.1a). We performed FTIR spectroscopy in attenuated total reflectance (ATR) mode (70)

in order to maximize the vibrational signal (schematic sample geometry is shown in the inset to Fig. 4.1b**)**.

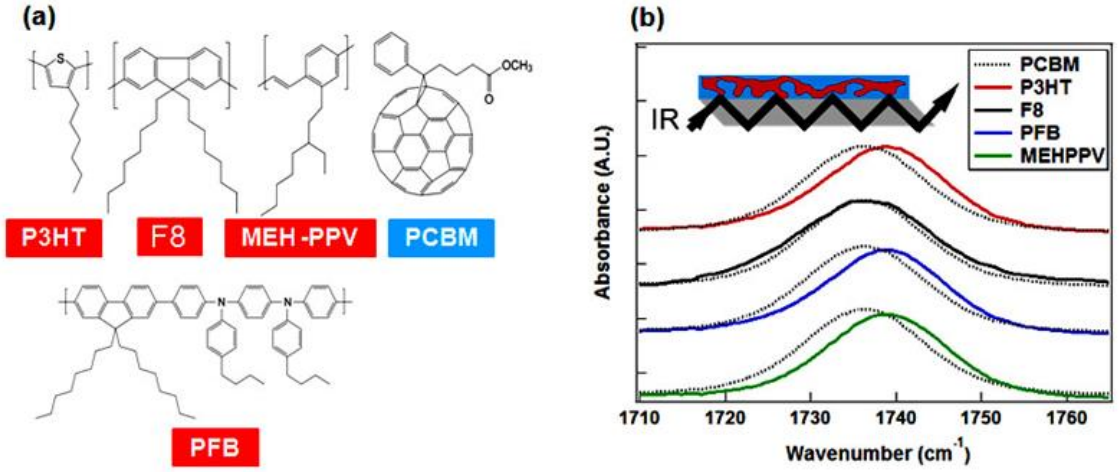

Figure 4.1: a) Schematic representation of a series of donor polymers together with the PCBM acceptor used as a reporter of the interfacial electric field b) PCBM carbonyl stretch in pristine films and after blending with donor polymers. The inset shows a schematic representation of the ATR-FTIR setup geometry. The IR beam bounce through the Si waveguide and the μm evanescent wave is used to probe the top film.

For example, the PCBM C=O stretch frequency blue-shifts by 2.5 cm^{-1} within a bulk heterojunction blend of poly 3-hexyl-thiophene (P3HT) (red curve in Fig. 4.1b), corresponding to an interfacial electric field (*E*) of 0.25 V/nm (based on a Stark tuning rate of 1 cm^{-1} per $10^8 V/m^1$ for the C=O stretch mode (71)). Previous UPS measurement of a planar P3HT/C_{60} interface (59) showed an increase in vacuum level energy of Δ = 0.6 eV upon deposition of C_{60} on the P3HT surface. Similar interfacial dipoles (0.5-0.6 eV)

have been recently reported for P3HT/PCBM bulk hererojunctions. Based on the values of E & Δ and assuming a planar heterointerface, we estimate an interfacial charge separation distance of $d = \Delta / (e \cdot E) = 2.4$ nm and an interfacial charge density of $\rho \cdot \varepsilon \cdot \varepsilon_0 \cdot e = 0.41$ unit charge/nm^2, where e is the electron charge, ε_0 is the vacuum permittivity, and ε (~3) is the average relative dielectric constant of P3HT and PCBM. In contrast, the C=O stretch frequency shows little shift when PCBM is blended with the polymer poly(9,9-di-*n*-octylfluorenyl-2,7-diyl) (F8) (black curve in Fig. 1b), again in agreement with previous UPS experiments showing $\Delta = 0$ for this type of interface (59). Blending PCBM with the semiconducting polymers poly(9,9′-dioctylfluorene-co-bis-*N*,*N*′-(4-butylphenyl)-bis-*N*,*N*′-phenyl-1,4-phenyldiamine) (PFB) and poly(2-methoxy-5-(2'-ethyl-hexyloxy)-1,4-phenylene vinylene) (MEH-PPV) also shifts the PCBM C=O stretch frequency by 2.2 cm^{-1} and 2.5 cm^{-1}, respectively (blue and green curves in Fig. 1b), and indicates interfacial electric fields similar in magnitude to those present in P3HT:PCBM blends. Stark effect spectroscopy allows us to simultaneously measure interfacial fields by using a different electric-field reporter group such as the cyano group (CN) in poly (5-(3,7-dimethyloctyloxy)-2-methoxy-cyanoterephthalylidene) (CN-MDMO-PPV), and the two measurements show excellent agreement.

4.2.2 Trapped Solvent and Solvent Annealing

FTIR spectroscopy is also a sensitive probe of the presence of residual solvent within the blended polymer:PCBM active layer. For example, we expect residual amounts of the 1,2-dichlorobenzene (ODCB) to reside in P3HT:PCBM films cast from this solvent (72), the presence of which can affect the PCBM carbonyl stretch frequency through

solvatochromism in a manner similar to the electric field induced by the P3HT interface. Small molecule additives have been previously shown to greatly influence the performance of bulk heterojunction solar devices (73).

The solvent ODCB is characterized by two vibrations in the FTIR spectrum at ~660cm^{-1} and 740cm^{-1} (indicated by arrows on the yellow curve in Fig. 4.2a). P3HT:PCBM films cast from ODCB still contain significant amounts of solvent after N_2 exposure for 15h at room temperature (red curve in Fig. 4.2a). Heating P3HT:PCBM films above ~80^{o}C for one hour greatly diminishes the amount of trapped solvent, with the FTIR signatures disappearing for temperatures above 80^{o}C (black, blue curves in Fig. 4.2a)

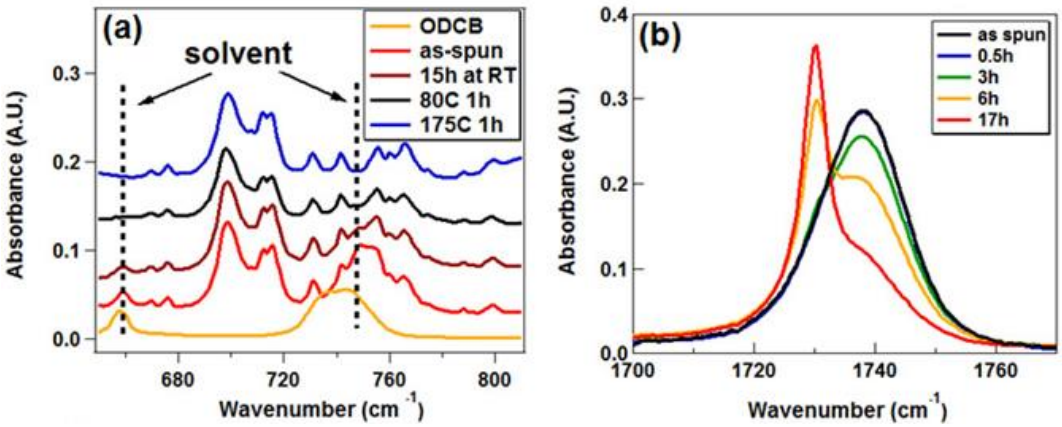

Figure 4.2: a) Comparison of the linear IR spectra of the solvent (ODCB) with the as spun and annealed P3HT (Mw=19KD) with PCBM blend b) PCBM carbonyl stretch in blends with P3HT solvent annealed with ODCB for different amount of times.

Organic semiconductor bulk heterojunction solar cells are often optimized by exposure to a saturated solvent vapor for an extended amount of time (74) – a process that

not only affects the internal blend structure but also the interfacial electric field. For example, exposure of a P3HT:PCBM active layer blend to ODCB produces a sharp, red-shifted PCBM C=O vibrational stretch peak at ~1730 cm^{-1}, accompanied by a decrease in intensity of the initial peak at 1738.4 cm^{-1} (Fig. 4.2b). The red-shifted C=O stretch peak results from the presence of the solvent, as has been well established for carbonyl-containing molecules (75). We can recover the initial PCBM C=O stretch peak position and intensity by annealing the film at $\geq 60^{o}C$ in vacuum to remove the incorporated solvent.

4.2.3 PCBM Crystallization upon Thermal Annealing

The photovoltaic performance of organic semiconductor bulk heterojunction solar cells depends critically on achieving suitable degrees of structural order across multiple length scales. For example in P3HT:PCBM bulk heterojunctions, the blend phase separates into distinct P3HT and PCBM domains under thermal annealing, while at the same time each of these components can separately crystallize. While the degree of P3HT and PCBM crystallinity is known to affect electrical and optical properties of the material (76), here we focus on its influence on the interfacial electric field.

GIXD measurements of PCBM thin films clearly show a transformation from amorphous to crystalline upon thermal annealing at temperatures above $150^{o}C$ (Figs. 4.3a, b). The crystalline PCBM shows a pattern of distinct diffraction spots (instead of rings), indicating crystallites having a preferential orientation with respect to the substrate surface (69). Previous x-ray diffraction measurements (77) of single crystals show that PCBM crystallizes in a monoclinic unit cell ($P2_1/n$) with four molecules per unit cell. We

may expect the PCBM molecules to pack in thin films in a fashion similar to single crystals, as has been previously observed in similar studies of thin pentacene films [78].

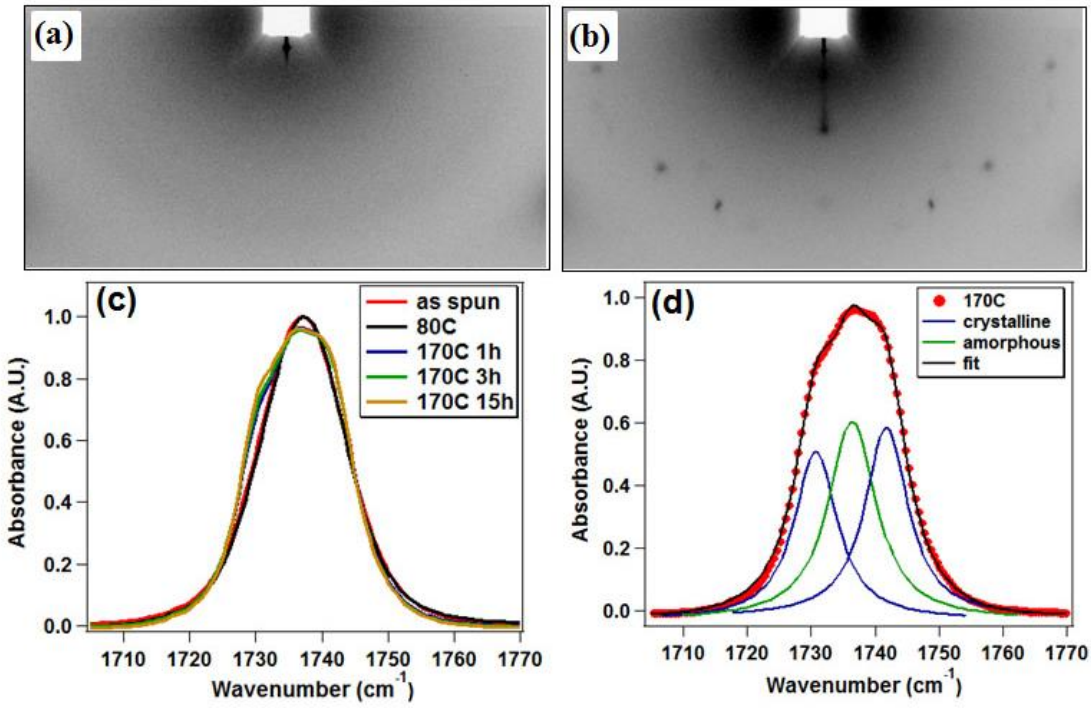

Figure 4.3: GIXD patterns of the neat PCBM films: as prepared (a), and annealed at 170^{o}C (b) c) PCBM carbonyl absorption spectra for as spun and annealed films at 80C, 170C for 1h, 3h and 15h. d) Deconvolution of the PCBM carbonyl stretch frequency with a sum of three Voigt functions corresponding to the amorphous (green) and crystalline (blue) domains from a neat PCBM film annealed at 170^{o}C.

Thermal annealing of a PCBM thin film (35 nm thick) changes the carbonyl stretch region of its FTIR spectra as well (Fig. 4.3c**)**, from which we can quantitatively assess the degree of PCBM crystallinity. The vibrational frequency of the C=O stretch mode in an amorphous PCBM film (υ_a= 1737.60±0.01 cm^{-1}) changes upon crystallization (170^{o}C for

1h), showing two additional spectral features on either side of the υ_a peak (at υ_{Cr1}= 1730.50±0.06 and υ_{Cr2}= 1741.80±0.05 cm^{-1}). We understand these two additional vibrational peaks as resulting from Davydov splitting (79) in crystalline PCBM domains. For a unit cell consisting of four asymmetric molecules, each vibrational energy level should split into four bands, but only two are dipole-allowed in optical absorption. Deconvolution of the C=O stretch vibrational frequencies of amorphous and crystalline domains (Fig. 4.3d) allows an estimation of the relative populations of amorphous (N_{Am}) and crystalline (N_{Cr}) PCBM domains:

$$\frac{N_{Am}}{N_{Cr}} = \frac{A_{Am}}{2\left(A_{Cr1} + A_{Cr2}\right)} \tag{4.1}$$

where $A_{Am,}A_{Cr1}$, and A_{Cr2} are the areas of the vibration peaks corresponding to the amorphous PCHM and the resulting Davydov splitting in the crystalline PCBM domains, while the factor of 2 in the denominator of Eq. (4.1) accounts for the two "dark" states in the crystalline domain. This analysis gives relative populations of crystalline domains of $\eta = N_{Cr}/(N_{Am}+N_{Cr})$ = 72% after one hour of annealing at 170^{o}C, further increasing to 76% after an additional 15 hours.

We use a similar combination of GIXD and FTIR spectroscopy to probe the PCBM internal structure in a P3HT:PCBM blend, thereby providing a new structural probe of these blend morphologies. GIXD measurements of an as-cast P3HT:PCBM blend show marked differences from those of the single-component PCBM (Fig. 4.3a), primarily due to the presence of three equally-spaced peaks oriented in the substrate perpendicular direction ($q_{\perp}$) (Fig. 4a).

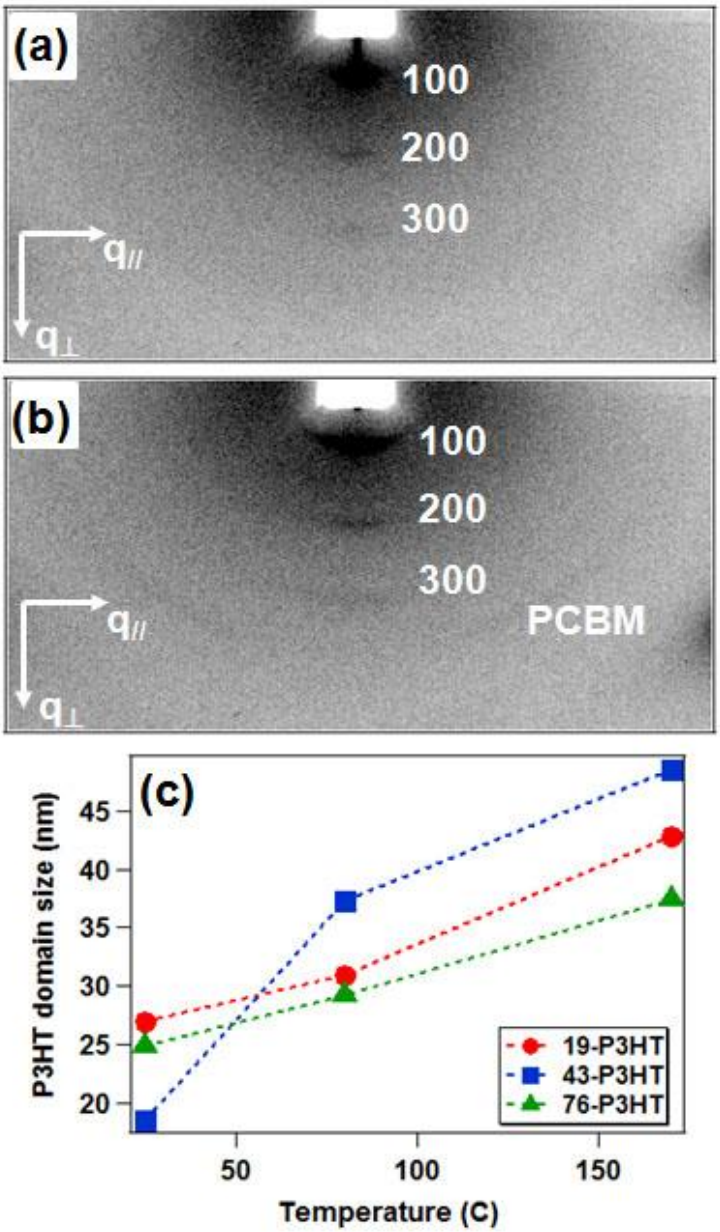

Figure 4.4: GIXD patterns of P3HT (Mw=43KD) and PCBM blends films: as prepared (a), and annealed at 170^{o}C (b). c) P3HT crystalline domain size calculated using Scherrer's equation.

These features are consistent with a lamellar chain stacking (with lattice constant 16.1Å) characteristic of crystalline P3HT (80). Annealing the P3HT:PCBM blend at

temperatures above 150^{o}C induces film structural changes, evidenced by the appearance of a diffraction ring at 0.46nm due to PCBM crystallization (Fig. 4.4b). Using a simple Scherrer analysis (81), we can estimate an average PCBM crystallite domain size of 15nm:

$$L = \frac{N\lambda}{\beta \cos\theta} \tag{4.2}$$

where N is a constant close to 1; λ is the wavelength of the incoming x-ray, β is the peak width at half maximum, and θ the scattering angle. The same analysis shows that the P3HT domain sizes are larger (Fig. 4.4c**)**, increasing in size from 20 to 40nm with higher annealing temperature. Similar GIXD patterns are measured for pure PCBM films and P3HT:PCBM blends spin coated on PEDOT:PSS coated surfaces (69, 82).

We can measure the volume fraction of crystallized PCBM by again deconvoluting the C=O stretch vibrational peak in the blend FTIR spectrum (Fig. 4.5). Our measurements are consistent with the P3HT inhibiting PCBM crystallization, as the PCBM reaches only 56% crystallinity after one hour of annealing (at 170^{o}C) and saturating at 68% after 15 hours. PCBM mixed with lower molecular weight P3HT (19K) crystallizes similarly to single-component PCBM films (72% crystallinity at 1 hour and 76% at 15 hours), while higher molecular weight P3HT (76K) slows the rate of crystallization (negligible crystallization at 1 hour and 68% at 15 hours).

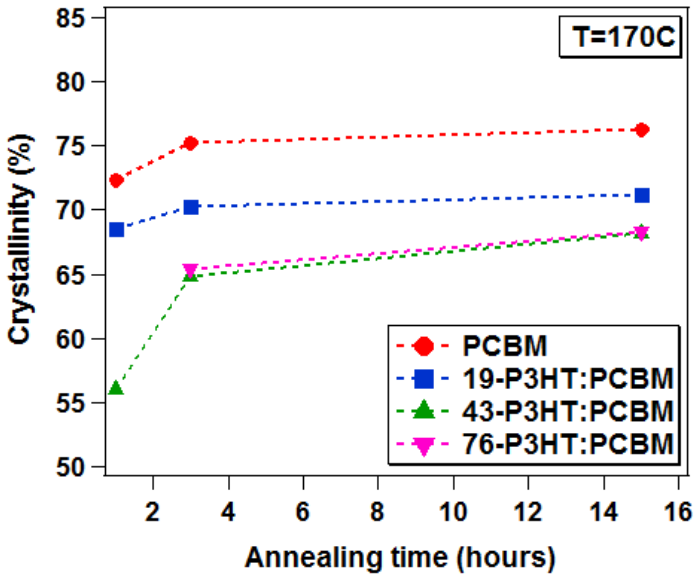

Figure 4.5: Degree of crystallinity calculated from the relative area of the vibrational frequencies corresponding to the crystalline and amorphous regions of Eq. 4.1.

4.2.4. The Interfacial Field and Crystallinity

Analysis of the PCBM C=O stretch frequency also facilitates a correlation between the degree of PCBM crystallinity and the strength of the interfacial electric field in P3HT:PCBM blend active layers. In a manner similar to single-component PCBM films, the frequency of the PCBM C=O stretch in blends with P3HT (M_w= 43 kD) changes as the film is thermally annealed (Fig. 4.6a). Blending PCBM with both lower (19kD) and higher (76kD) molecular weight P3HT produces qualitatively similar behavior (Fig. 4.6).

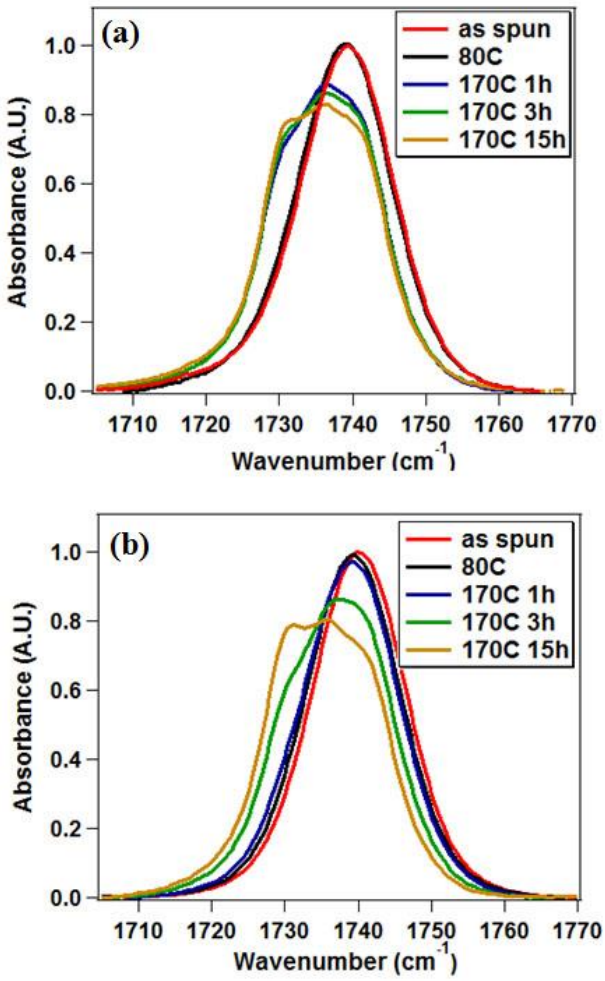

Figure 4.6: Normalized FTIR spectra in the region of the carbonyl stretch for P3HT (19KD) (a) and (76KD) (b) blends with PCBM annealed at different temperatures.

The blend data are consistent with PCBM crystallizing at temperatures above 150^{o}C (similar to single-component PCBM, section 2.3), and we can extract PCBM C=O vibrational frequencies corresponding to both amorphous (υ_a) and crystalline regions using a fitting procedure with a sum of three Voigt functions (one for the remaining

amorphous PCBM, and two for the crystalline regions). Our data (Fig. 4.7b) show that blending PCBM with P3HT shifts the carbonyl frequency from 2.2 to 3.1 cm^{-1} (green triangles for P3HT M_w= 43 kD) compared to single-component PCBM (red dots), and indicate the presence of an interfacial electric field (Fig. 4.7b).

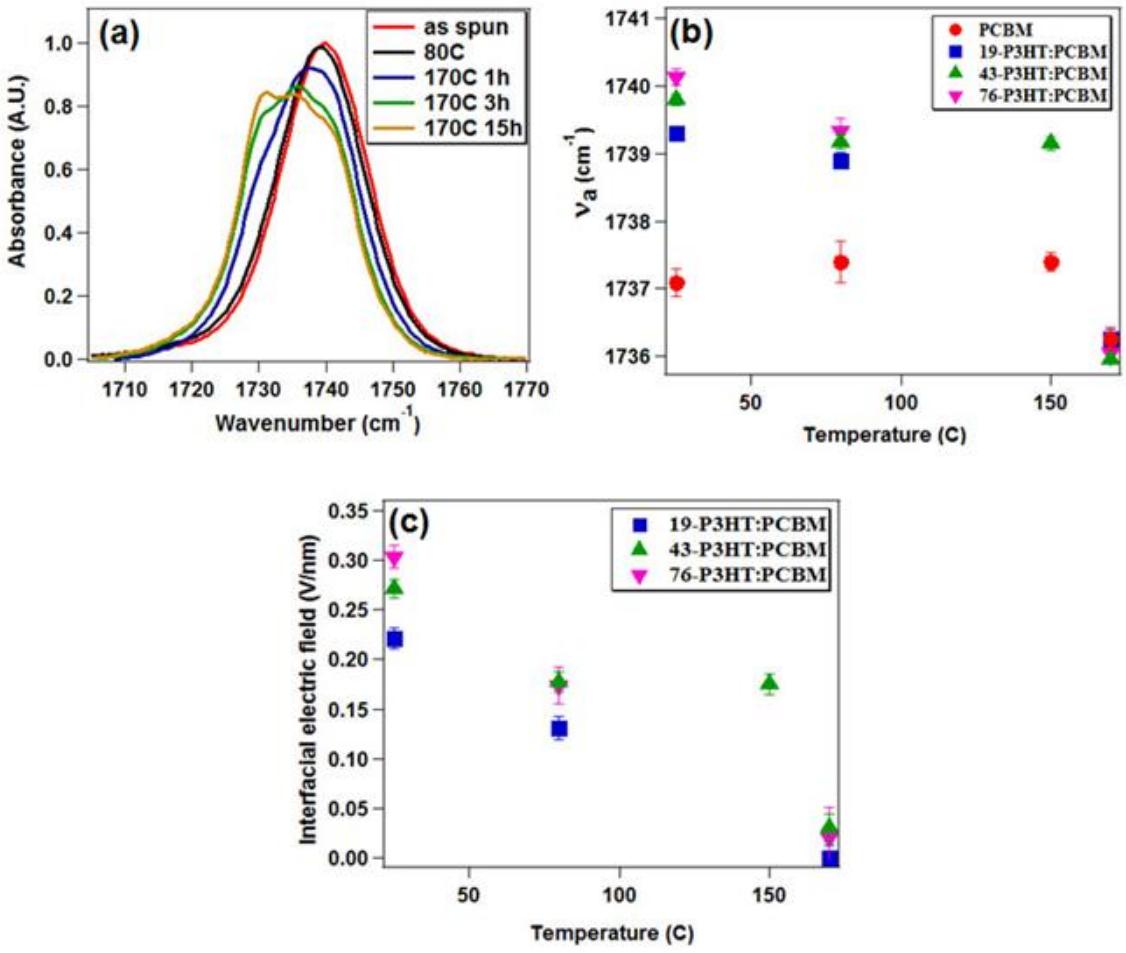

Figure 4.7: Normalized IR spectra in the region of the carbonyl stretch for P3HT (Mw=43KD) and PCBM blends (a). b) Carbonyl vibrational frequency of the amorphous PCBM in the pure film and blends as a function of the annealing temperature and the calculated interfacial field (c)

We calculate the interfacial electric field from the measured vibrational frequency shift using a carbonyl Stark tuning rate of $1cm^{-1}$ per 10^8V/m (71). The electric field at the P3HT/PCBM interface decreases when the as-cast film at room temperature is annealed at 80°C, likely due to the removal of solvent from the film. It stays constant until 150°C and then decreases dramatically to negligible value with further annealing at 170°C when extensive PCBM crystallization occurs (Fig. 4.7c). In P3HT:PCBM films annealed at 170°C, we observe similar field strengths at P3HT interfaces with amorphous and crystalline PCBM regions as well (Fig.4.8).

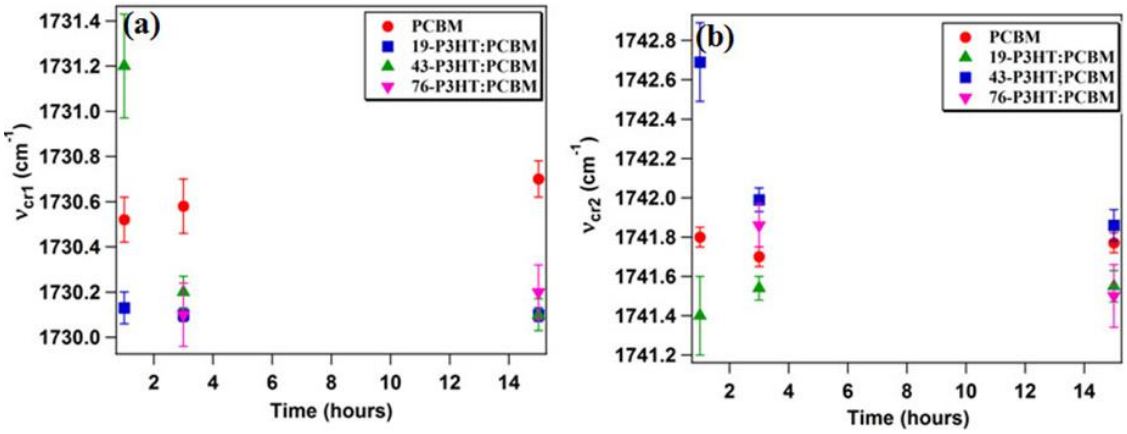

Figure 4.8: Upon crystallization after annealing at 170°C, two additional features at approx 1730.5 (υ_{Cr1}) (a) and 1741.8 cm^{-1} (υ_{Cr2}) (b) appear as shoulders of the carbonyl amorphous peak. The exact position of the crystalline and amorphous vibrational frequencies can be determined by deconvoluting the absorption with a sum of three Voigt functions. The two crystalline vibrations are not well defined after annealing at 170°C for one hour therefore the imprecision in determining the exact vibration frequencies corresponding to the crystalline domains. After annealing for three hour the interfacial field can be estimated to be approx 0.05 V/nm.

We can qualitatively understand the relationship between interfacial field and local PCBM crystallinity as follows: crystallization creates more electronic delocalization and polarization, which can more effectively screen the interfacial electric field and, thus decrease the measured Stark frequency shift.

4.2.5 Implications for Solar Cell Performance

Thermal processing of the organic semiconductor active layer blend is an important tool for improving and optimizing solar cell performance, and can affect PCBM electron- and P3HT hole mobilities through increasing crystallinity and blend phase separation. (83,84) The formation of ordered domains at the P3HT:PCBM interface increases the extent of delocalization of the hole and electron wavefunctions, and thereby facilitates dissociation of charge-transfer excitons. Measurements here show that increasing crystallinity also decreases the interfacial electric field, thus modifying the electronic energy alignment.

Increasing the thermal annealing temperature for a P3HT:PCBM organic solar cell (1:1 P3HT:PCBM, P3HT M_w= 38K) from 150^{o}C to 170^{o}C dramatically changes the illuminated device current-voltage *J-V* characteristic (Fig. 4.9).

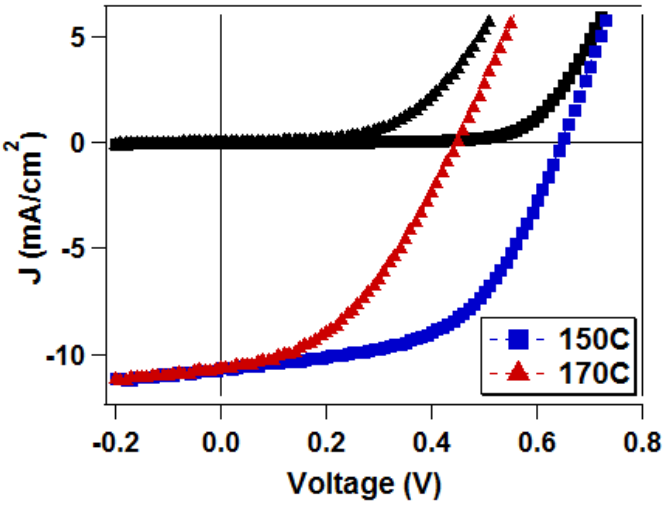

Figure 4.9: J-V characteristic for the P3HT (Mw=38KD) and PCBM blend devices annealed at 150 and 170^{o}C

Optimal devices processed at 150^{o}C perform with overall power conversion efficiency of 3.7%, providing a short circuit current (J_{sc}) of 10.7mA/cm^2 and supporting an open circuit voltage of V_{oc}= 0.62 V (100 mW/cm^2 simulated AM1.5G illumination, calibrated using a certified KG5 filtered silicon reference cell) (85). The 20 degree increase in annealing temperature crystallizes the PCBM component (Fig. 4.3b) and reduces V_{oc} by 35% (from 0.62V to 0.4V) and the associated device power conversion efficiency to 2.1%. The device J_{sc} remains largely unchanged upon PCBM crystallization, suggesting a lesser role for the interfacial field in charge separation and supporting Monte-Carlo simulations showing that polaron-pair dissociation is field-independent under the device operating conditions (49).

Although there is no general consistent understanding of the origin of V_{oc} in organic bulk heretojuction solar cells, several loss mechanisms have been recently identified and quantified. Initial studies portrait V_{oc} as solely dependent on the D/A interface gap ($\delta_{D/A}$) defined as the difference between the LUMO of the electron accepting material (LUMO(A)) and the HOMO of the electron donor material (HOMO(D)) (86). However, charge transfer across the D/A interface that appears as a result of differences in chemical potential between the D and A determines the appearance of an interfacial dipole Δ with magnitudes ranging from 0.1 to 1eV which widens the interfacial band gap (50). Important loss mechanisms affecting the V_{oc} include charge carrier recombination and entropic losses due to heterogeneity across the device. With present knowledge, the V_{oc} can be expressed as:

$$V_{OC} = \frac{1}{e}\left(\delta_{D/A} + \Delta\right) - \frac{k_B T}{e} \ln\left(\frac{n_e n_h}{N_C^2}\right) - \frac{1}{e}\varepsilon_L \qquad (4.3)$$

where the second term represents the recombination loss (87,55) and the last term is the sum of all additional free energy losses during carrier transport.

When the annealing temperature is increased from 150 to 170^{o}C, we observe a change in V_{oc} of -0.22V. The change in interfacial electric field is -0.14 V/nm, corresponding to an interfacial dipole voltage change of Δ/e = -0.34 V (based on the estimated charge separation distance of d = 2.4 nm obtained in section 2.1). Thus the observed decrease in the interfacial dipole fields is consistent with the observed decrease in the V_{oc} upon crystallization of the PCBM at an annealing temperature of 170°C. This correlation suggests that the change in the interfacial dipole is likely a significant contribution to the

change in the device V_{oc}. The last two terms actually account for ~0.12 V relative increase in V_{oc}, suggesting less recombination and other losses for the higher annealing temperature of 170^{o}C than those at 150^{o}C. While a complete and quantitative understanding of V_{oc} under OPV device operating conditions is not yet possible at the present time, our demonstration of measuring interfacial electric field at buried interfaces in the complex bulk D/A heterojunction represents an important step in achieving this goal.

4.3. CONCLUSIONS

We have used vibrational Stark effect spectroscopy to quantitatively measure the interfacial electric fields at organic donor/acceptor bulk heterojunction interfaces and to determine the degree of crystallinity in P3HT/PCBM blend films. The interfacial electric field of ~0.2 V/nm in P3HT:PCBM blend films (after removal of trapped solvent) remains constant as a function of annealing temperature in the range of 80^{o}C to 150^{o}C. When the annealing temperature is further increased from 150^{o}C to 170^{o}C, the interfacial electric field vanishes and this is accompanied by the crystallization of PCBM domains. The decrease in interfacial electric field is correlated with the change in open circuit voltage in P3HT:PCBM bulk heterojunction solar cells. These results establish vibrational Stark effect spectroscopy as a viable method in quantifying the critically important electric field at buried D/A interfaces in bulk heterojunction OPVs.

4.4 EXPERIMENTAL

PCBM was used as received from Aldrich and dissolved in 1,2-dichlorobenzene to a concentration of 20 mg/mL. P3HT (Mw = 19, 43 and 76 kD) was purchased from Reike Metals and dissolved in 1,2-dichlorobenzene (20 mg/mL). The P3HT with Mw=38 KDa used in the photovoltaic devices was purchased from American Dye Source. Solutions were mixed in a 1:1 weight ratio and spin coated onto Si/SiO_2 or ZnSe substrates at 700 rpm. Thicknesses of neat PCBM films and P3HT:PCBM blends were measured using ellipsometry (J. A.Wollam Co., Inc.) and were found to be 35 and 110nm respectively.

We carried GIXD experiments at beamline X6B, National Synchrotron Light Source, Brookhaven National Laboratory, USA using the x-ray energy of 15.8 keV. The focused beam of 0.25 mm vertical x 0.5 mm horizontal was incident on the sample film at an angle of 0.4 degrees. The diffraction pattern was collected using a CCD detector (Princeton Instruments), with a 120 x 120 mm image area (2084x2084 pixels). Raw images were corrected for dark count, flat field, and spatial distortion using calibration frames obtained with a ^{55}Fe source and a brass plate machined with 1 mm holes on a square grid of 2.54 mm pitch. Detector to sample distance, typically ~ 240mm, was calibrated using measurements of Ag behenate powder.

All spectroscopic measurements were performed on a Nicolet 6700 FTIR spectrometer. The IR beam was passed through a potassium bromide (KBr) window into a glove box and was focused by a concave mirror (f = 15 cm) into the crystal waveguide

(ATR). The exiting IR light was re-collimated and focused into a liquid nitrogen cooled Mercury Cadmium Telluride (MCT) infrared detector.

Bulk heterojunction devices were fabricated on indium tin oxide (ITO) coated glass. A ~40 nm thick PEDOT:PSS layer was deposited on ITO by spincoating at 5,000 RPM, followed by 10 min bake at 140^{o}C on a preheated plate. The device active layers were spin coated P3HT:PCBM blends. The top Al contact (100nm thick) was deposited by thermal evaporation at 10^{-6} Torr. Before contact deposition, the blends were annealed at 150 and 170^{o}C in a vacuum oven.

J-V curves were measured using a custom-modified Rucker-Kolls electrical probe station and an Agilent 4156C Precision Semiconductor Parameter Analyzer. The photocurrent was measured under AM1.5 G 100 mW/cm^2 (1 SUN) from a 150 W solar simulator (Oriel 96000).

Thermal annealing of the P3HT:PCBM blend films at room temperature was performed in a N2 filled glove box, while annealing at higher temperatures was performed in a vacuum oven.

Chapter 5: *Mapping Electric Field Distributions in Biased Organic Bulk Heterojunctions under Illumination by Nonlinear Optical Microscopy*

In this chapter†, we apply electric field induced second harmonic generation (EFISH) microscopy to quantitatively map the spatial distributions of electric fields in lateral organic bulk heterojunctions. We investigate two model BHJ systems: poly(3-hexylthiophene) (P3HT) and phenyl-C61-butyric acid methyl ester (PCBM) and poly(4,4-dioctyldithieno(3,2-b:2',3'-d)silole)-2,6-diyl-alt-(2,1,3-benzothiadiazole)-4,7-diyl) (PSBTBT) and PCBM. In the former (P3HT/PCBM) we observe a non-uniform field distribution due to the presence of a depletion region adjacent to the electron collecting electrode, while in the latter (PSBTBT/PCBM) we find a linear potential drop. We discuss the origins of uniform or non-uniform field distributions in organic BHJs and illustrate the power of EFISH microscopy in probing space charge accumulation in organic semiconductor devices.

5.1 INTRODUCTION

The photo-to-electric power conversion efficiency of organic photovoltaics (OPVs) has improved dramatically in recent years to as high as 10% (6). High performance OPVs

† *Much of the content of this chapter has been reprinted with permission from:*

> J. D. Morris, T. L. Atallah, C. J. Lombardo, H. Park, A. Dodabalapur, and X.Y. Zhu, "Mapping electric field distributions in biased organic bulk heterojunctions under illumination by nonlinear optical microscopy," *Appl. Phys. Lett*. **102**, 033301 (2013) © 2013 American Institute of Physics.

typically consist of bulk heterojunctions (BHJs) in which the active region is a mixture of an electron donor and an electron acceptor material phase separated on the nanometer scale (21). Modeling of a BHJ-OPV cell typically assumes that a built-in or applied bias drops linearly across the active material between two electrodes (88,54), but this assumption often fails for a number of reasons. For example, the common presence of contact resistance (89) at a metallic electrode introduces voltage drop at the interface, while asymmetric mobility in electron and hole carriers or an imbalance in carrier generation and collection rates leads to space charge build-up (29). These non-uniform spatial distributions of electric fields can be detrimental to device performance, such as high charge carrier recombination rates and low fill factors in BHJ OPV devices (90). Experimental determination of such electric field distributions is of central importance to the understanding and design of organic BHJ devices. Past studies have mainly relied on indirect approaches, such as current-voltage characteristics, impedance spectroscopy, and time-of-flight measurements (91,92) but the extraction of the electric field distribution requires considerable modeling based on various assumptions.

Ideally, we would like to directly determine the spatial distributions of electric fields in operating BHJ devices. One successful approach is scanning Kelvin probe microscopy (SKPM) (93-95), but this technique is limited to open devices with the active layers exposed to the probe tip. Device degradation is a serious concern when the measurement is carried out under conditions other than ultrahigh vacuum. Besides, deviation of the surface potential from that of the bulk organic material is a potential complication (60). Here we apply electric field induced second harmonic generation (EFISH) microscopy

(96-99) to map the electric field distributions in operating organic bulk heterojunctions. We use the lateral bulk heterojunction (LBHJ), which is a poor geometry for OPV efficiency but a good model system for the understanding of key mechanistic problems, such as space charge build-up, and charge carrier recombination (100). We investigate two model systems: the widely used electron acceptor phenyl-C61-butyric acid methyl ester (PCBM) mixed with poly(3-hexylthiophene) (P3HT) or poly(4,4-dioctyldithieno(3,2-b:2',3'-d)silole)-2,6-diyl-alt-(2,1,3-benzothiadiazole)-4,7-diyl) (PSBTBT). The former (P3HT/PCBM) (101) is the most extensively studied material system for bulk heterojunction solar cells while the latter (PSBTBT/PCBM) (102) represents an emerging class of low bandgap semiconducting polymers for high efficiency OPVs.

EFISH is a special case of second harmonic generation where the conversion of two incident photons of frequency ω to a single photon of frequency 2ω depends on the strength of an electric field present within a system (34). The total second harmonic signal in the presence of an electric field is given by (35):

$$\begin{aligned} I^{2\omega} &= \left| E_0^{2\omega} e^{i\varphi_0} + E_{EFISH}^{2\omega} e^{i\varphi_{EFISH}} \right|^2 \\ &= \left(E_0^{2\omega}\right)^2 + \left(E_{EFISH}^{2\omega}\right)^2 + 2E_0^{2\omega} E_0^{2\omega} \cos(\varphi_0 - \varphi_{EFISH}), \end{aligned} \tag{5.1}$$

where $E_0^{2\omega}$ and φ_0 are the second harmonic field and the corresponding phase in the absence of any EFISH contributions, where $E_{EFISH}^{2\omega}$ and φ_{EFISH} are the second harmonic field and the corresponding phase arising from the DC electric field, and $I^{2\omega}$ is

the total second harmonic intensity. Generally a quantitative determination of $E_{EFISH}^{2\omega}$ from measurement of $I^{2\omega}$ alone is not possible because the phase difference between $E_0^{2\omega}$ and $E_{EFISH}^{2\omega}$ is unknown. However, under the dipole approximation (103), $E_0^{2\omega}$ is zero for a material of inversion symmetry (such as the bulk heterojunction used here) and, if the surface contribution to $E_0^{2\omega}$ is also sufficiently small, the total second harmonic signal is approximated by:

$$I^{2\omega} = \gamma \left| E_{EFISH}^{2\omega} \right|^2 = \gamma \left| \chi_{ijkl}^{(3)} E^{\omega} E^{\omega} E^{DC} \right|^2 = \gamma \left| \chi_{eff}^{(3)} \right|^2 \left(I^{\omega} \right)^2 \left(E^{DC} \right)^2 \qquad (5.2)$$

where γ is a constant that depends on the experimental geometry and includes the appropriate Fresnel coefficients, $\chi_{ijkl}^{(3)}$ is the third order nonlinear susceptibility, $\chi_{eff}^{(3)}$ is the effective fourth rank nonlinear susceptibility tensor, I^{ω} is the intensity of the incident light at the fundamental frequency, and E^{DC} is the electric field.

5.2 EXPERIMENTAL

We fabricated lateral organic heterojunction devices on glass substrates that were pre-patterned with asymmetric electrodes: aluminum (Al) cathodes (50 nm thick) and gold (Au) anodes (50 nm thick). A schematic of this device geometry is shown in Fig.5.1b. We chose these two metals to minimize reverse bias carrier injection in the bulk heterojunction (104). The inter-electrode spacing was L = 15 or 20 μm for the devices used here. After a brief etch in phosphoric acid to remove aluminum oxide from the Al electrodes and rinsing with acetone, we spin-coated each BHJ thin film at 800 rpms for

60 seconds. For P3HT:PCBM, we used a 1:1 (by weight) solution of 10 mg/ml of both PCBM and P3HT in chlorobenzene. The device was then annealed at 140 °C for 20 minutes. For PSBTBT:PCBM we spin-coated from a solution of 10mg/ml PSBTBT and 18mg/ml PCBM in chlorobenzene. After spin-coating we heated the PSBTBT:PCBM films to 80 °C for 30 minutes to remove any remaining chlorobenzene solvent.[105] Finally we encapsulated each device with a microscope coverslip and optical epoxy, which is cured at 125 °C for 10 minutes. All steps of the film preparations were performed in a dry nitrogen environment. Fig. 4.1a shows schematically a top view of the lateral BHJ device.

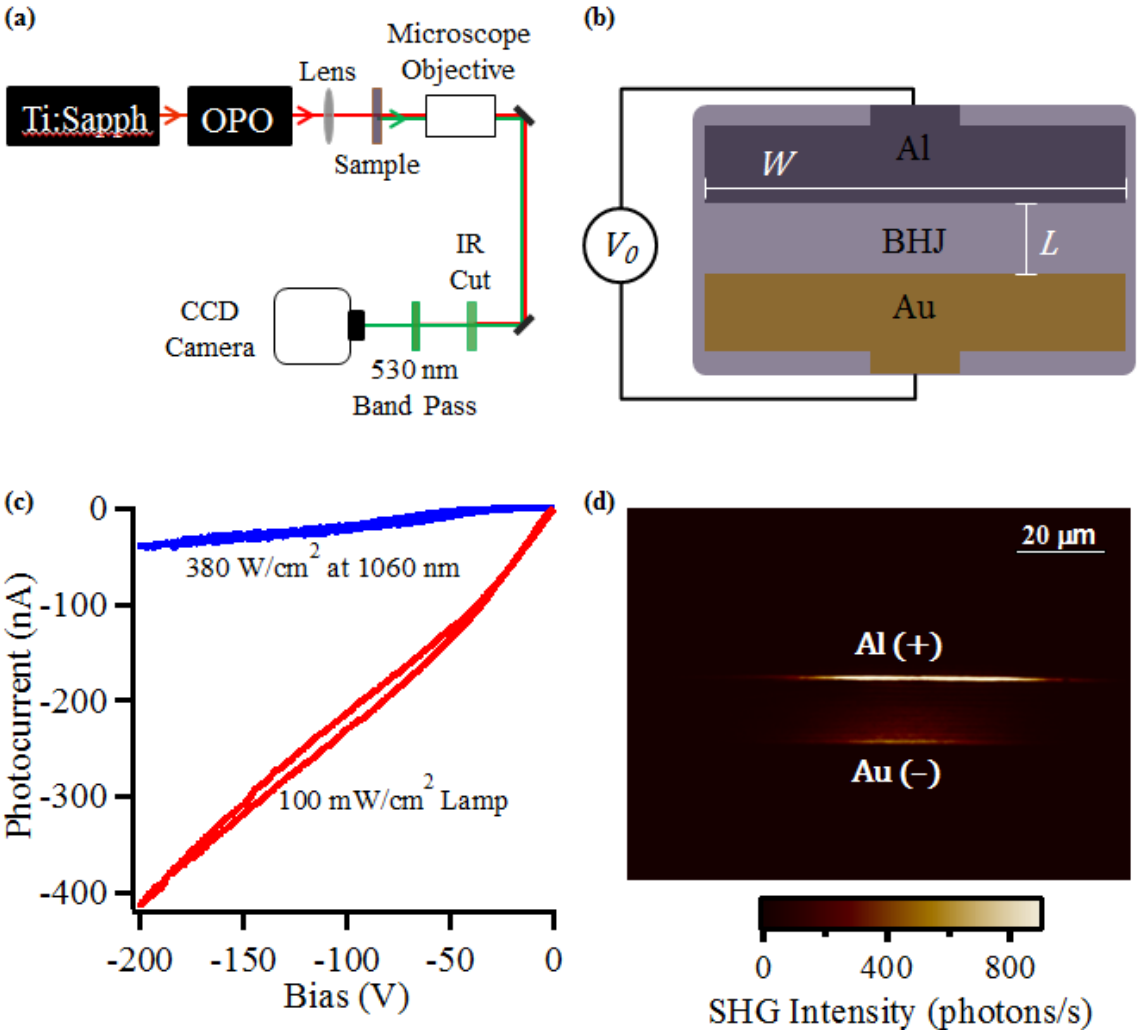

Figure 5.1: a) The EFISH microscopy optical layout. b) Schematic of the LBHJ device geometry. The W/L ratio for these channels was 50. c) Typical photocurrent curves (light current – dark current) for LBHJs. In this case PSBTBT:PCBM is shown under illumination by one sun and the fundamental beam at 1060 nm. The current density within the area illuminated by the fundamental beam is actually equivalent to the current density across the entire length of the channel at 1-Sun since the fundamental beam only illuminates 1/10th of the LBHJ channel. d) An EFISH microcopy image of PCBM:P3HT at -200V. The high intensity adjacent to the aluminum contact indicates a depletion layer has formed in this device. The nature of this depletion layer is clarified in Fig. 5.4 and associated discussion

All EFISH microscopy images were taken in transmission mode with a fundamental beam at 1060 nm (~120 fs, 76 MHz, pulse energy ~ 2 nJ) generated by an optical parametric oscillator (Coherent Mira-OPO) pumped by a Ti:sapphire oscillator (Coherent Mira HP), Fig. 5.1c. The 1060 nm laser beam was focused by an f = 10 cm lens to a diameter of 80 μm on the device surface. The second harmonic signal at 530 nm was imaged by a microscope objective (Mitutoyo 20X) and recorded on an EM-CCD camera (Andor Technology 897E) which was cooled to 170 K thermoelectrically. Using appropriate bandpass and/or cutoff filters, we obtained images either at 1060 nm (fundamental) or 530 nm (EFISH).

5.3 RESULTS AND DISCUSSION

Details on the current/voltage (I/V) characteristics of the lateral BHJ device under illumination have been published elsewhere (100). Fig. 5.1c compares I/V profiles (blue) of the PSBTBT:PCBM lateral BHJ under the EFISH imaging condition (illumination at 1060 nm) with that illuminated under one-Sun (halogen lamp calibrated against solar simulator). In the absence of light, leakage current from the device is negligible in the voltage range probed here. Since both PSBTBT and PCBM are transparent at 1060 nm, we attribute the observed photocurrent to two-photon absorption. Taking into account geometric factors, i.e., percentage of illuminated area by the focused laser beam, we estimated that the photocurrent density generated under the 1060 nm laser beam is equivalent to that under the illumination of one-Sun.

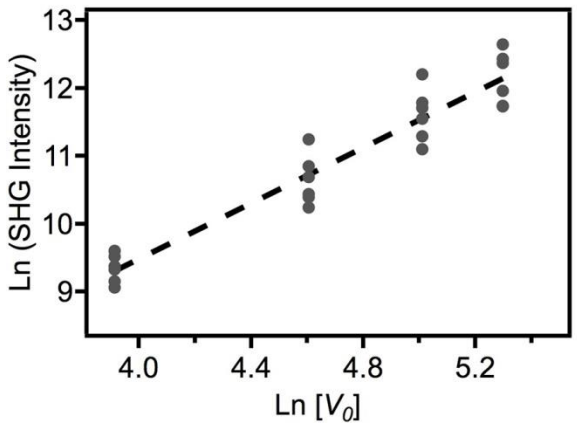

Figure 5.2: A log/log plot of integrated SHG intensities (dots) from EFISH images versus applied bias votalges for a P3HT:PCBM device. Least-square linear fit (dashed line) to the data gives a slope of 2.0 ± 0.3.

A typical EFISH image of a P3HT:PCBM device (bias = -200 V) is shown in Fig. 5.1d. A careful inspection of the image reveals interference fringes parallel to the edge of the channel in the SHG image; these interference fringes result from edge diffraction and are common features of microscopy with coherent light (96). To establish EFISH microscopy as a quantitative tool for the mapping of electric field, we integrate the second harmonic signal across each channel (in the direction of the applied field) and plot the integrated signal against bias voltage (V_o) in Fig. 5.2. This log/log plot shows a linear relationship with a slope of 2.0 ± 0.3, as predicted by equation 5.2. Note that the electric field in equation 5.2, E^{DC}, is proportional to the bias voltage, V_o. We now turn to the analysis of spatial electric field distributions from EFISH images. We first focus on PSBTBT/PCBM devices. As discussed earlier, photocurrent generation due to two-photon absorption of probe laser light at 1060 nm is equivalent to the same device under one-Sun illumination.

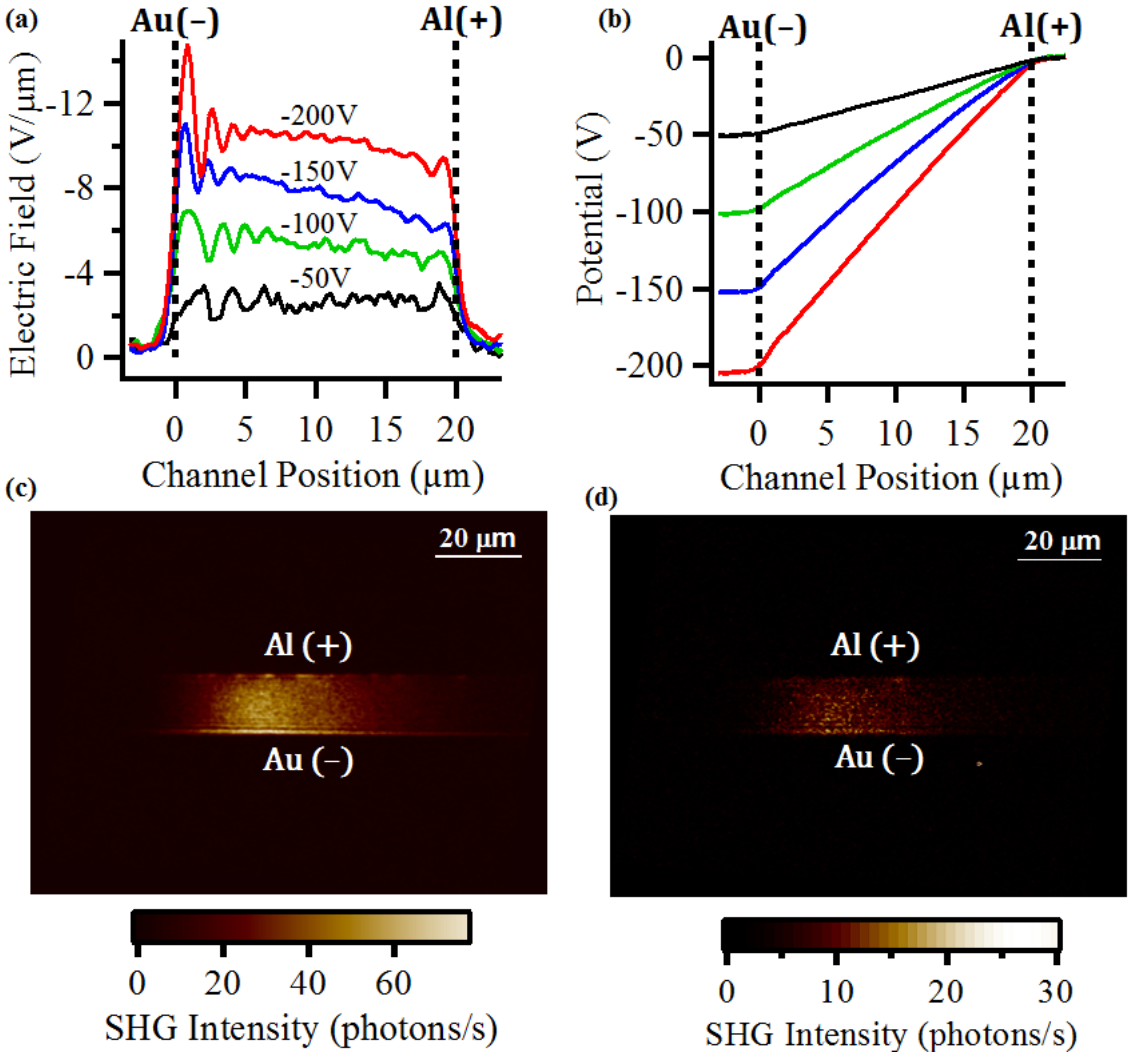

Figure 5.3: a) The electric field distribution across the PSBTBT/PCBM channel at various applied biases. b) The linear bias drops across PSBTBT/PCBM at a range of applied biases c) PSBTBT:PCBM EFISH image at -200V d) PSBTBT:PCBM at -100V.

Fig. 5.3a shows spatial profiles of the square-root SHG intensity ($\sqrt{I^{2w}}$) across the L = 20 μm channel for the PSBTBT/PCMB device under different bias voltages (-50 to -200V), with positive on the Al electrode and negative on the Au electrode. Each profile was obtained from an image (shown for V_o = -200 V and V_o = -100 V Fig. 5.3c and 5.3d)

averaged for ~30 s. We find that $\sqrt{I^{2w}}$, and thus the electric field E^{DC} ($= a \times \sqrt{I^{2w}}$), is nearly constant across the channel (except for the edge diffraction fringes). To quantitatively obtain the calibration factor (α), we integrate $a \times \sqrt{I^{2w}}$ over the length (L) of the channel and the result should give V_0 in each case. This factor allows us to convert $\sqrt{I^{2w}}$ to the electric field, as shown by the y-axis in Fig. 5.3a. The constant electric field also corresponds to a linear voltage drop between the electrodes, as shown in Fig. 5.3b obtained from the integration of the electric profile for each bias voltage in Fig. 5.3a. The ability to directly obtain the electric field profile across the channel between the two electrodes allows us to unambiguously conclude that there is negligible space charge accumulation. Note that the presence of contact resistance, if any, at the PSBTBT/PCBM-metal interface cannot be ruled out. Previous measurement showed that the contact voltage drop in a spatial region of 10^2 nanometers (106), which is below the spatial resolution of the EFISH microscope. This contrasts with features due to space charge accumulation that are expected to span several micrometers (107). The absence of space charge accumulation in the PSBTBT/PCBM lateral BHJ solar cell is in excellent agreement with previous transport measurements (108,109) that showed well matched electron and hole mobility in PSBTBT/PCBM. The EFISH images and, thus, electric field distributions, are stable with prolonged measurements over several hours, indicating the stability of the PSBTBT/PCBM bulk heterojunction under illumination.

In contrast to the PSBTBT/PCBM device, we find that the electric field distribution in the P3HT/PCBM device deviates from the constant field profile and is unstable over time.

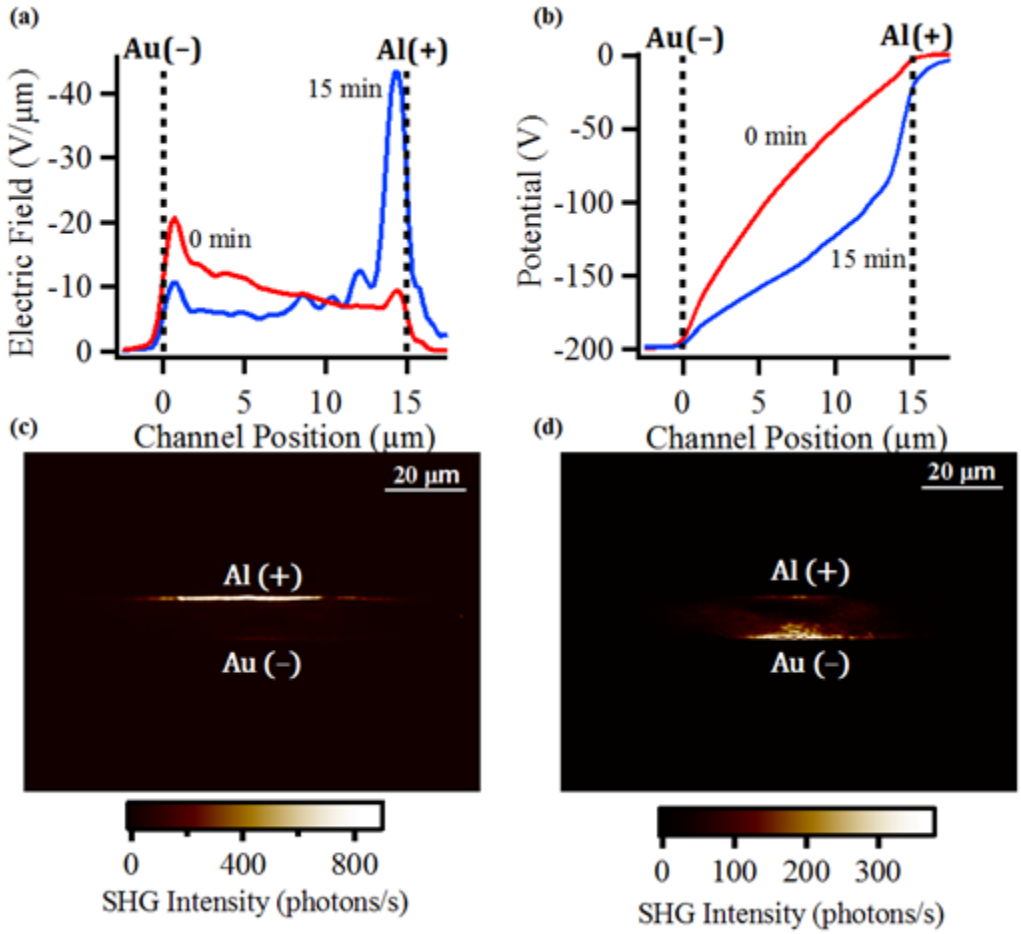

Figure 5.4: a) The electric field distribution across the P3HT:PCBM channel in the initial 60s of laser exposure and after 15 minutes of laser exposure. b) The bias drop corresponding to the electric fields shown in a. c) The initial EFISH microscopy image of P3HT:PCBM at -200V. Note that a small depletion layer has already formed where the laser beam was most intense. d) P3HT:PCBM image at -200V after 15 minutes of laser exposure

Fig. 5.4a compares the electric field distribution obtained for the first 30 seconds (red) to that after a total of 15 minutes (blue) under laser radition. The initial electric field

distribution is relatively constant, with enhanced field near the Au electrode, suggesting the presence of a small hole injection barrier. However, after 15 minutes under laser irradiation, the electric field shifts dramatically, with a field drop at the Al electrode more than five times than those at other locations in the device. This dramatic change in electric field is also evident in the integrated data, i.e., electric potential with distance across the channel Fig. 5.4b. The nearly linear potential profile (red) becomes highly nonlinear (blue) after 15 minutes, with a nearly 50% voltage drop near the Al electrode. Fig.5.4c and d shows EFISH images of the P3HT/PCBM device at t = 0 and 15 minutes of illumination.

The electric field or potential profile obtained after 15 minutes of illumination is consistent with the formation of a depletion layer adjacent to the Al (electron-collecting) electrode. Previous measurements based on impedance spectroscopy have suggested the presence of a charge depletion region adjacent to the electron-collecting electrode in photo-oxidized P3HT:PCBM devices (110). It was argued that photo-oxidation introduced negatively charged electron traps that serve to screen the positively biased Al electrode. The direct observation of a space charge region near the Al electrode with time in Fig. 5.4 is consistent with photo-oxidation, which may result from moisture trapped in the device. It is clear that photo-oxidation has begun even in the initial measurement since some accumulation has already occurred at the Al electrode. Note that the 2-photon absorption cross section at 1060 nm by P3HT:PCBM is ~30% of that for PSBTBT:PCBM. Thus, in terms of photocurrent, the P3HT:PCBM device under EFISH imaging condition is equivalent to that 30% of 1-Sun illumination.

The development of such a space charge region attributed to photo-oxidation, even in a sealed device used here, cautions against the interpretation of experimental measurements for P3HT:PCBM bulk heterojunctions where photo-oxidation may be even more likely to occur. Indeed, previous measurements of the P3HT:PCBM bulk heterojunction by KPFM and time-of-flight showed significant voltage drops localized to the electron-collecting electrodes (91,93). It is likely that, in these previous studies, considerable photo-oxidation already occurred before the data were collected.

The results presented above establish EFISH microscopy as a quantitative tool in mapping the spatial distribution of electric fields in organic semiconductor devices. We apply the technique to the characterization of two prototypical organic bulk heterojunction material systems, PSBTBT:PCBM and P3HT:PCBM, that are widely used in OPVs. In PSBTBT:PCBM, we show the absence of space charge builtup due to the well-balanced electron and hole mobilities. In the widely used P3HT:PCBM bulk heterojunction, we show that the often reported space charge region near the electron-collecting electrode is not intrinsic, but rather develops with photo-irradiation attributable to photo-oxidation. Both examples demonstrate the significant value of EFISH microscopy in the mechanistic understanding of organic semiconductor devices.

Chapter 6: *Quantifying Space Charge Accumulation in Organic Bulk Heterojunctions by Nonlinear Optical Microscopy*

6.1 INTRODUCTION

In this chapter, we apply electric field induced second harmonic generation (EFISH) microscopy to directly observe and quantify space charge accumulation in operating organic bulk heterojunction photovoltaic cells (OPVs) comprised of poly(4,4-dioctyldithieno(3,2-b:2',3'-d)silole)-2,6-diyl-alt-(2,1,3-benzothiadiazole)-4,7-diyl) (PSBTBT) mixed with phenyl-C61-butyric acid methyl ester (PCBM). We adjust the relative electron and hole mobility within these blends by altering the relative composition of PSBTBT and PCBM, and observe dramatic shifts in space charge accumulation. In these devices we observe that PSBTBT rich devices showing strong electron accumulations ($2.8x10^{14}$ e^-/cm^3) and PCBM rich devices showing strong hole accumulations ($5.5x10^{14}$ h^+/cm^3).

6.1.1 Background

In 1971 Goodman and Rose predicted that significant mismatch between electron and hole mobilities in a photovoltaic cell would give rise to space charge accumulation (SPA) and deviation from charge neutrality during device operation (28). At sufficiently high charge carrier generation rates, such space charge regions give rise to a fundamental limit on the photocurrent which can be extracted from an operating device (29). Further SCA can increase charge carrier recombination and reduce device efficiency (111).

In 2005, Blom and coworkers reported indirect evidence of space charge accumulation regions, and the associated fundamental limit on photocurrent, within OPVs with considerable mismatch in charge carrier mobilities (29). Using current-voltage measurements, they determined the dependence of photocurrent on the generation rate reduces to $G^{3/4}$ in the space charge limited regime, just as predicted by Goodman and Rose in 1971. Unfortunately the dependence of photocurrent on the generation rate can be affected by a variety of factors including charge carrier recombination (30).

In the present work, we implement electric field induced second harmonic generation (EFISH) microscopy to directly observe and quantify SCA in active organic bulk heterjunction devices comprised of phenyl-C61-butyric acid methyl ester (PCBM) and poly(4,4-dioctyldithieno(3,2-b:2',3'-d)silole)-2,6-diyl-alt-(2,1,3-benzothiadiazole)-4,7-diyl) (PSBTBT). PSBTBT is part of an emerging class of organic semiconductors, which are comprised of a donor-accopor blocks along the polymer backbone which allow for a reduced optical bandgap for optimal solar harvesting (102).

6.1.2 Lateral Bulk Heterojunctions

We employ a lateral bulk heterojunction geometry (LBHJ) (shown in Fig. 6.1) which is a poor geometry for OPV efficiency but allows for direct optical investigation with EFISH microscopy. Direct determination of the charge carrier density throughout the photovoltaic cell provides unambiguous information about SCA in these devices. Recently Ooi et. al simulated the SCA within such a device geometry using a drift-diffusion model (107,112).

Essentially these simulations showed that a strong accumulation of electrons is expected adjacent to the electron colleting electrode, and, similarly, an accumulation of holes is expected adjacent to the hole collecting electrode. The relative magnitude of these accumulations depends on the relative mobility of the two charge carriers. If the electron mobility is greater than the hole mobility, then the number of holes accumulated near the hole collecting contact will be greater than the quantity of electrons accumulated near the electron collecting contact. This mismatch in accumulation balances the collection rate of electrons and holes at equilibrium by altering the electric field in the vicinity of charge collection.

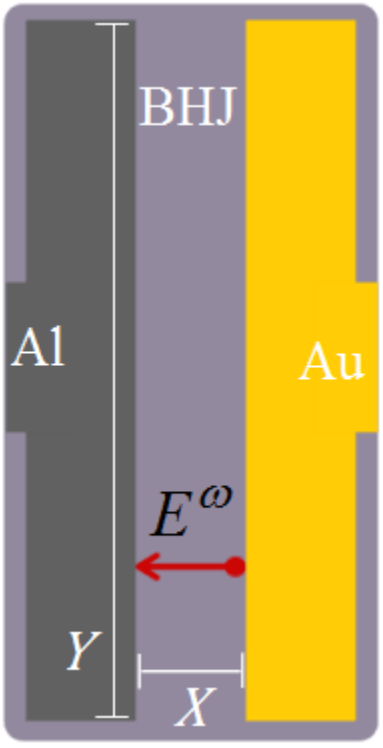

Figure 6.1: A schematic of the sample geometry used in the EFISH microscopy experiments. The red line represents the polarization of the incident electric field. The channel length in the x direction is 20 μm while the electrode width in the y direction is 1 mm.

6.1.3 EFISH Microscopy

EFISH is a special case of second harmonic generation where the efficiency of converting two photons at frequency ω to one photon at frequency 2ω depends on strength of a constant electric field present within the systems (96). As shown in the previous chapter, the second harmonic response from our lateral bulk heterojunction systems is given by:

$$I^{2\omega} = \gamma \left| E^{2\omega}_{EFISH} \right|^2 = \gamma \left| \chi^{(3)}_{ijkl} E^{\omega} E^{\omega} E^{DC} \right|^2 = \gamma \left| \chi^{(3)}_{eff} \right|^2 \left(I^{\omega} \right)^2 \left(E^{DC} \right)^2 \quad (6.1)$$

where γ is a constant that depends on the experimental geometry and includes the appropriate Fresnel coefficients, $E_{FEFISH}^{2\omega}$ is the electric field arising from EFISH contributions, $\chi_{ijkl}^{(3)}$ is the fourth rank nonlinear susceptibility tensor, E^{ω} is the incident optical field at frequency ω, $\chi_{efl}^{(3)}$ is the effective fourth rank nonlinear susceptibility tensor, I^{ω} is the intensity of the incident light at the fundamental frequency and finally E^{DC} is the electric field.

In order to effectively interpret our second harmonic intensity, we need to understand how E^{DC} is mapped to our intensity, $I^{2\omega}$, by $\chi_{ijkl}^{(3)}$. In general a fourth rank tensor, such as $\chi_{ijkl}^{(3)}$, will have 81 individual elements. However, for centrosymmetric materials (such as the organic bulk heterojunctions under investigation here), only seven nonzero terms remain. The total second harmonic polarization at 2ω in each direction (the coordinate system used here is defined in Fig. 6.1) is given by (37),

$$P_x^{2\omega}(2\omega) = \chi_{xxxx}^{(3)} E_x(\omega) E_x(\omega) E_x^{DC}(0) + \chi_{xyyx}^{(3)} E_y(\omega) E_y(\omega) E_x^{DC}(0), \tag{6.2}$$

$$P_y^{2\omega}(2\omega) = \chi_{yyyy}^{(3)} E_y(\omega) E_y(\omega) E_y^{DC}(0) + \chi_{yxxy}^{(3)} E_x(\omega) E_x(\omega) E_y^{DC}(0), \tag{6.3}$$

$$\begin{aligned} P_z^{2\omega}(2\omega) &= \chi_{zzzz}^{(3)} E_z(\omega) E_z(\omega) E_z^{DC}(0) + \chi_{zyyz}^{(3)} E_y(\omega) E_y(\omega) E_z^{DC}(0) \\ &+ \chi_{zxxz}^{(3)} E_x(\omega) E_x(\omega) E_z^{DC}(0), \end{aligned} \tag{6.4}$$

where χ_{ijkl} is a specific tensor element, $E_i(\omega)$ is the incident field at frequency ω with i polarization, and where E_i^{DC} is the electric field in the i direction within the material of

interest. Conveniently if the incident electric field $E_i(\omega)$ is strongly polarized in the x-direction we can reduce Eq.3.8 to 3.10 to,

$$P_x^{2\omega}(2\omega) = \chi_{xxxx}^{(3)} E_x(\omega) E_x(\omega) E_x^{DC}(0), \tag{6.5}$$

$$P_y^{2\omega}(2\omega) = \chi_{yxxy}^{(3)} E_x(\omega) E_x(\omega) E_y^{DC}(0), \tag{6.6}$$

$$P_z^{2\omega}(2\omega) = \chi_{zxxz}^{(3)} E_x(\omega) E_x(\omega) E_z^{DC}(0). \tag{6.7}$$

Further, we can neglect any contributions from Eq. 6.7 as any z-polarized light will propagate in a direction perpendicular to the incident beam and will not be detected. From Eq. 6.6 and 6.7 we can see that by selecting the correct polarization we can easily map both E_x^{DC} and E_y^{DC} separately. When we observe the x-polarized light our second harmonic intensity will be given by:

$$I^{2\omega} \approx \gamma \left| \chi_{xxxx}^{(3)} \right|^2 \left(I^{\omega}\right)^2 \left(E_x^{DC}\right)^2, \tag{6.8}$$

and by selecting the y-polarized light our second harmonic intensity will be given by:

$$I^{2\omega} \approx \gamma \left| \chi_{yxxy}^{(3)} \right|^2 \left(I^{\omega}\right)^2 \left(E_y^{DC}\right)^2, \tag{6.9}$$

In our LBHJ devices, however, we find contributions from E_y^{DC} to be negligible compared to the measurements of E_x^{DC}.

6.2 EXPERIMENTAL

All EFISH microscopy images were taken in transmission mode with a fundamental beam at 1060 nm (~120 fs, 76 MHz, pulse energy ~ 2 nJ) generated by an optical parametric oscillator (Coherent Mira-OPO) pumped by a Ti:sapphire oscillator

(Coherent Mira HP). The 1060 nm laser beam was focused by an f = 10 cm lens to a diameter of 80 µm on the device surface. The second harmonic signal at 530 nm was imaged by a microscope objective (Mitutoyo 20X) and recorded on an EM-CCD camera (Andor Technology 897E) which was cooled to 170 K thermoelectrically. Using appropriate bandpass and/or cutoff filters, we obtained images either at 1060 nm (fundamental) or 530 nm (EFISH). Fig. 6.2 shows the experimental setup implemented for these studies which now includes a polarizer. (Note that while no polarizer was used for the investigations in chapter 5, we later confirmed that the contribution arising from the electric field in x direction is three orders of magnitude higher than those arising from the electric field in y direction).

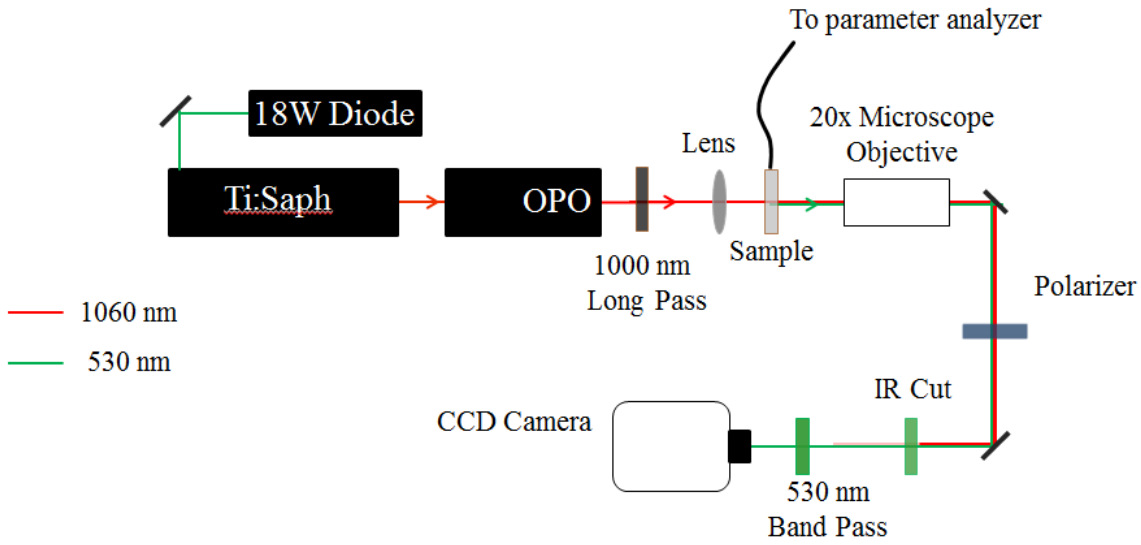

Figure 6.2: A schematic of the optical layout implemented in these EFISH microscopy studies.

We fabricated lateral organic heterojunction devices on glass substrates that were pre-patterned with asymmetric electrodes: aluminum (Al) cathodes (50 nm thick) and gold (Au) anodes (50 nm thick). A schematic of this device geometry is shown in Fig.6.1. We chose these two metals to minimize reverse bias carrier injection in the bulk heterojunction (104). The inter-electrode spacing was L = 20 μm for the devices used here. After a brief etch in phosphoric acid to remove aluminum oxide from the Al electrodes and rinsing with acetone, we spin-coated each BHJ thin film at 800 rpms for 60 seconds. Each film was comprised of PSBTBT:PCBM in varying ratios of 2:3, 3:1 and 1:3, which we spin-coated from a solution of 12mg/ml PSBTBT and 18mg/ml PCBM, 22.5mg/ml PSBTBT and 7.5mg PCBM, and finally, 7.5mg PCBM and 22.5mg/ml PCBM respectively, all in chlorobenzene. After spin-coting, we heated the PSBTBT:PCBM films to 80 °C for 30 minutes to remove any remaining chlorobenzene (105). Finally we encapsulated each device with a microscope coverslip and optical epoxy, which is cured at 125 °C for 10 minutes. All steps of the film preparations were performed in a dry nitrogen environment.

The increased interelectrode distance in lateral bulk heterojunctions significantly reduces the built in electric field. In order to simulate the built in field, we apply a voltage of 200V with the negative potential on the aluminum electrode and the positive potential on the gold electrode. In order to take a typical EFISH image we apply this fixed voltage and integrate the second harmonic intensity for 30 seconds.

6.3 RESULTS AND DISCUSSION

6.3.1 Solar Illumination

Details on the current/voltage (I/V) characteristics of the lateral BHJ device under illumination have been published elsewhere (100). Fig. 6.3a compares I/V profiles (blue) of the 2:3 PSBTBT:PCBM lateral BHJ under the EFISH imaging condition (illumination at 1060 nm) with that illuminated under one-Sun (halogen lamp calibrated against solar simulator). In the absence of light, leakage current from the device is negligible in the voltage range probed here. Since both PSBTBT and PCBM are transparent at 1060 nm, we attribute the observed photocurrent to two-photon absorption. Taking into account geometric factors, i.e., percentage of illuminated area by the focused laser beam, we estimated that the photocurrent density generated under the 1060 nm laser beam is equivalent to that under the illumination of one-Sun. Thus all measurements in this chapter take place with a charge carrier generation rate that is similar to solar conditions.

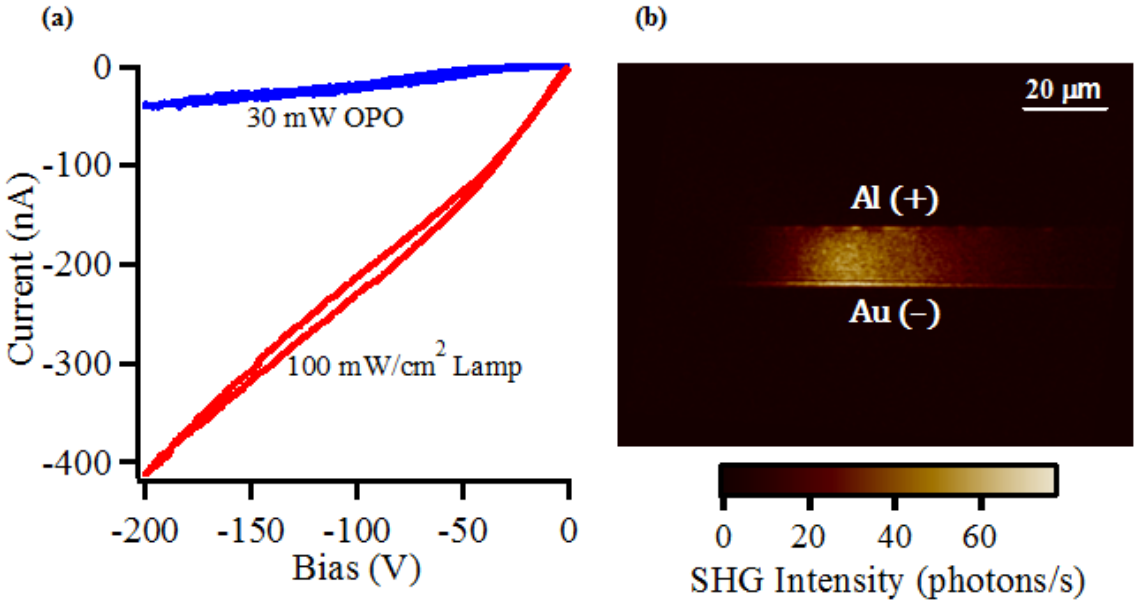

Figure 6.3: a) Typical photocurrent curves (light current – dark current) for LBHJs. In this case 2:3 PSBTBT:PCBM is shown under illumination by one sun and the fundamental beam at 1060 nm. The current density within the area illuminated by the fundamental beam is actually equivalent to the current density across the entire length of the channel at 1-Sun since the fundamental beam only illuminates ~1/10th of the LBHJ channel. b) An EFISH microcopy image of 2:3 PSBTBT:PCBM at -200V. All intensity, in this case, is polarized in the x-direction and hence the intensity arises from the x-component of the electric field as defined by Fig.6.1.

6.3.2 EFISH Profiles

A typical EFISH image of the 2:3 PSBTBT:PCBM device is shown in Fig. 6.3b. In this case, all second harmonic intensity is polarized in x-direction as defined by Fig. 6.1, thus the intensity is proportional to the square of the electric field pointing from the aluminum to the gold electrode. In order to quantitatively calibrate our second harmonic intensity, we take the square root of our second harmonic intensity and integrate this intensity across the channel in the direction of the applied field. In each case the result should be our applied field.

After quantitatively calibrating our second harmonic intensity to the electric field, we take the average of many line profiles across our device channel. The average electric field profile across the device imaged in Fig. 6.3b is shown in Fig. 6.4.

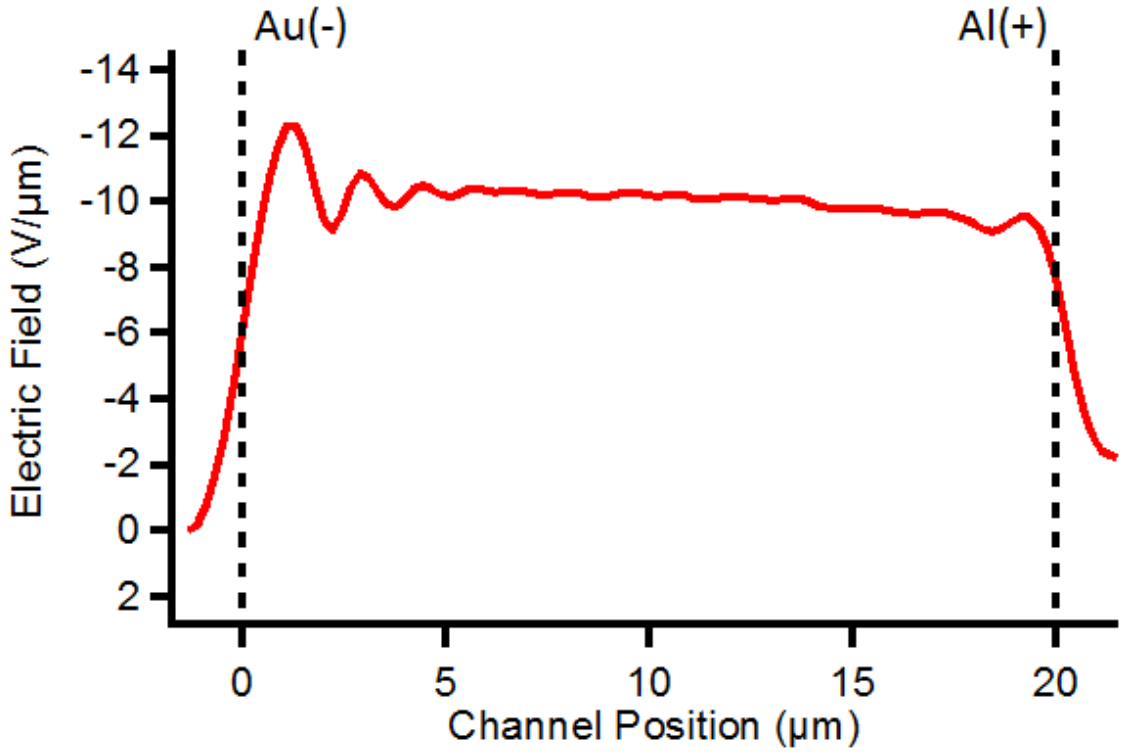

Figure 6.4: Electric field profile across the 2:3 PSBTBT:PCBM device as a function of channel position.

In the EFISH profile of 2:3 PSBTBT:PCBM, we see a periodic oscillation adjacent to the gold electrode which is attributed to knife edge diffraction, a common artifact in coherent microscopy. Importantly the electric field across the profile is relatively constant. This implies that there is limited charge carrier accumulation throughout the device, which suggests a well-balanced electron and hole mobility in this system.

In order to vary the effective electron and hole mobility, we made two additional devices, one with a 1:3 ratio of PSBTBT:PCBM and a second with a ratio of 3:1 PSBTBT:PCBM. Since the domains of electron donor allow the for the migration of holes back to the hole collecting contact, we expect a reduced concentration of electron donor (as in 1:3 PSBTBT:PCBM) to reduce the effective hole mobility. Similarly a reduction in the concentration of the electron acceptor (as in 3:1 PSBTBT:PCBM) should reduce the effective electron mobility. This phenomenon has been shown in field effect transistor measurements of donor acceptor blends (113). The shift in the available pathways for electrons and holes in these different blends is illustrated in Fig. 6.5.

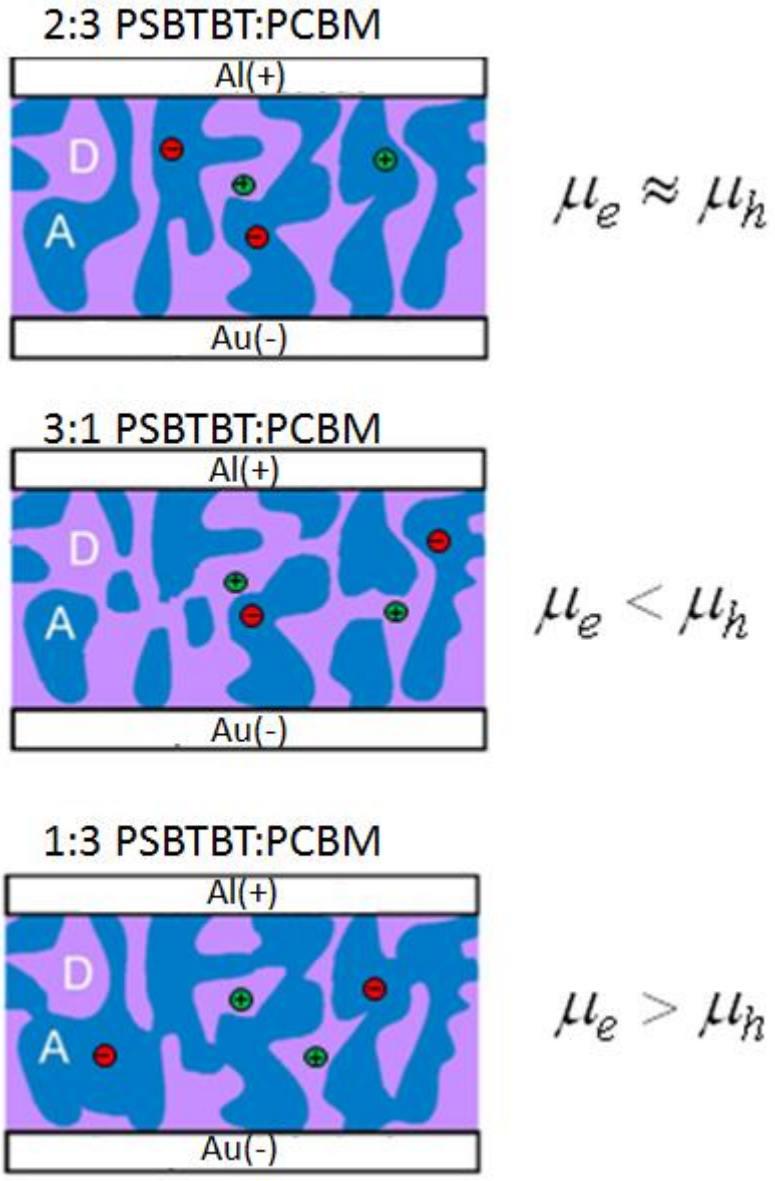

Figure 6.5: An idealized illustration of the three different donor/acceptor blends showing the expected change in the relative effective electron hole mobility due that varying availability of migration paths back to the appropriate electrode.

In Fig. 6.6a, we see the electric field profile of 1:3 PSBTBT:PCBM. We can clearly see a field enhancment near the gold electrode corresponding to an accumulation of holes.

Additionally we see a small enhancement of the electric field adjacent to the aluminum electrode which corresponds to a minor accumulation of electrons.

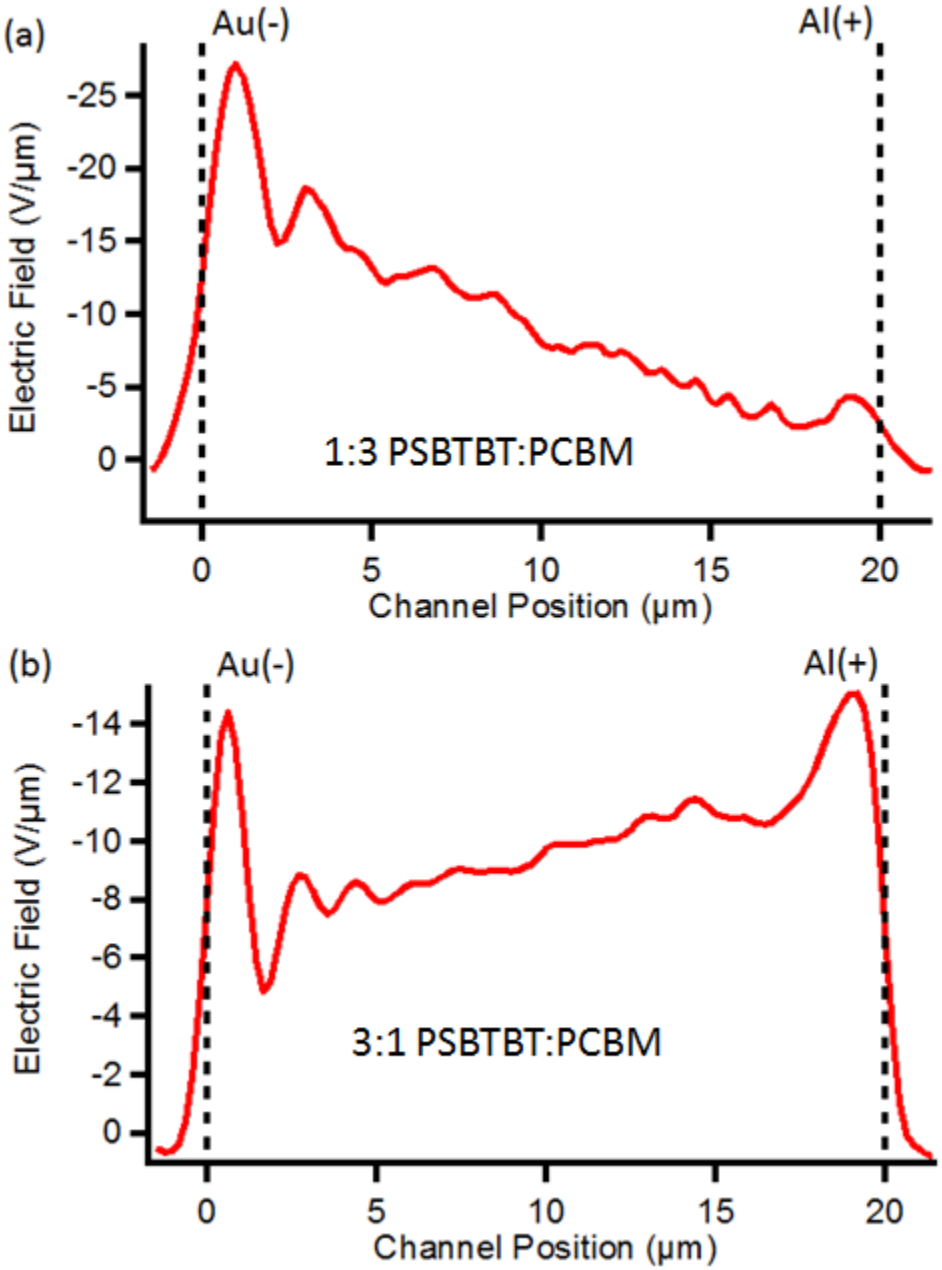

Figure 6.6: a) The electric field profile of 1:3 PSBTBT:PCBM as a function of channel position. b) The electric field profile of 3:1 PSBTBT:PCBM as a function of channel position.

The stronger enhancement near the hole collecting electrode is consistent with an electron mobility that is greater than the hole mobility as expected from the reduced availability of hole migration pathways in this electron acceptor rich film.

In Fig. 6.5b, we also observe field enhancements consistent with the expected mobility shift. In 3:1 PSBTBT:PCBM, we see a strong field enhancement adjacent to the electron collecting contact and a slightly smaller field enhancement adjacent to the hole collecting contact. From this qualitative examination is seems clear that we are directly observing SCA within our organic bulk heterojunctions.

6.3.3 Quantifying Space Charge Accumulation

In order to quantify the magnitude of these SCAs, we apply the differential form of Gauss's law in 1-D,

$$\frac{dE_x}{dx} = \frac{\rho}{\varepsilon}, \tag{6.10}$$

where E_x is the x component of the electric field (the same quantity we obtained through the calibration of our EFISH profiles), ρ is the free charge density, and ε is the permittivity of the material under investigation (taken to be three times the permittivity of free space for the donor/acceptor blends used here). We can readily substitute the relative hole and electron concentration and obtain,

$$\frac{dE_x}{dx} = \frac{q}{\varepsilon}\left(p(x) - n(x)\right) \tag{6.11}$$

where p(x) is the concentration of holes, and n(x) is the concentration of electrons and q is the elementary charge. Eq. 6.11 implies that wherever the slope of our electric field

profiles is positive we have SCA comprised of holes, and conversely, wherever the slope of these profiles is negative we have an accumulation of electrons.

In order to quantify the charge accumulation throughout our device we apply a best fit line to different regions of our electric field profiles and take the slope as an approximation of the average derivative throughout each region. We than use equation 6.11 to estimate the concentration, and carrier type, within each portion of the LBHJ channel.

Due to the limited resolution of our optical microscope (~.5 μm), the intensity at the electrode edge rises over some finite distance. We begin quantifying charge carriers at .5 μm in order to avoid this region directly adjacent to the electrode where intensity changes due to the limited resolution of our microscope. Further the typical special extent of these SCAs directly adjacent to the electrodes is roughly 3 or 4 μm (100, 107). For these two reasons, we choose .5 to 4 μm for our first region and 16 to 19.5 μm for our third region. Finally we quantify the accumulation between these two ranges, from 4 to 16 μm. The results of this process are summarized in Table 6.1.

Space Charge Accumulation (x 10^{14}) Electrons/Holes			
Composition	**.5 to 4 µm**	**4 to 16 µm**	**16 to 19.5 µm** **(18 to 19.5 µm)**
3:1 PSBTBT:PCBM	**2.1 ± 0.9 h^+/cm^3**	**0.5 ± 0.02 e^-/cm^3**	**2.8 ± 0.2 e^-/cm^3**
1:3 PSBTBT:PCBM	**5.5 ± 1.1 h^+/cm^3**	**1.6 ± 0.03 h^+/cm^3**	**0.5 ± 0.2 e^-/cm^3** **(2.0 ± 0.5 e^-/cm^3)**
2:3 PSBTBT:PCBM	**1.0 ± 0.3 h^+/cm^3**	**0.1 ± 0.06 h^+/cm^3**	**.21 ± .7 h^+/cm^3** **(0.5 ± 0.2 e^-/cm^3)**

Table 6.1: A summary of the magnitude and carrier type of each space charge accumulation region throughout each of the three devices under investigation. Accumulations of electrons (holes) are shown in red (green).

First we will consider only the regions directly adjacent to the electrodes. These data quantitatively confirm that the electron mobility is greater than the hole mobility in our 1:3 PSBTBT:PCBM device as the hole accumulation is significantly greater than the electron accumulation in this blend ($5.5x10^{14}$ h^+/cm^3 adjacent to the hole collecting contact vs $0.5x10^{14}$ e^-/cm^3 adjacent to the electron collecting contact) Though an examination of the electric field profile for 1:3 PSBTBT:PCBM suggests that the spatial extent of the electron SCA is significantly smaller than 4 µm in this case, and, indeed, when we quantify the electron accumulation from 18 to 19.5 µm we observe a charge density of $2.0x10^{14}$ e^-/cm^3.

In the case of the 3:1 PSBTBT:PCBM device, we again confirm that the SCA is consistent with the expected relative mobility of the electron and hole. Though in this case the observed difference is significantly less ($2.1x10^{14}$ h^+/cm^3 vs $2.8x10^{14}$ e^-/cm^3). The presence of two strong accumulations suggests that the mobilities are less mismatched in the case of the 3:1 PSBTBT:PCBM than in the case of 1:3 PSBTBT:PCBM. In fact previous simulations have shown that, while moderately mismatched mobilities give rise to two regions with considerable accumulation, stronger mismatch results in the strong accumulation of just the slower carrier. Our data suggest that the 1:3 PSBTBT:PCBM is approaching this regime with only a single carrier accumulating (107, 112).

Finally in the 2:3 PSBTBT:PCBM, blend we see that we have a slightly faster electron mobility. Again we see that the spatial extent of the electron accumulation in this device is considerably smaller than 4 μm. In fact, if we fail to shrink the region over which we quantify the SCA, we get the result that holes are accumulating adjacent to the hole collecting electrode. In actually this result is due to the considerable quantity of holes which occupy the central region of this device which has been inadvertently averaged in with the electron SCA.

SCA can only occur in regions where some fraction of charge carriers are collected (28). This suggests that separated electrons and holes have some chance of collection even in the center of our device from distances spanning over 10 μm. This is consistent with previous scanning photocurrent measurements which have shown some charge collection from the center of PSBTBT:PCBM LBHJ devices (114).

As expected, the accumulation within the center of these devices is more concentrated when we examine the 3:1 and 1:3 PSBTBT:PCBM devices. We see, again, that the electric field within these regions is altered by SCA which balances the collection rate of electrons and holes from the center of these devices.

6.4 CONCLUSIONS

In summary, we have shown that EFISH microscopy is capable of generating quantitative electric field maps across active organic bulk heterojunction photovoltaic cells. From these electric field maps, we can readily quantify the excess charge within any region of these devices. Further we have shown direct evidence of SCA within organic bulk Heterojunctions which results from a mismatch in electron and hole mobility. We find that the SCAs are on the order of 10^{14} charges/cm^3. Finally, we have shown, that such space charge can be found at great distances from the contacts, implying charge carriers can be collected from dsitances over 10 μm.

References

1. G. R. Timilsina, L. Kurdgelashvili, P. A. Narbel, *Renewable Sustainable Energy Rev.* **16**, 449 (2012).

2. H. Akamatu, H. Inokuchi, Y. Matsunaga, *Nature* **173**, 168 (1954).

3. C. W. Tang, *Appl. Phys. Lett.* **48**, 183 (1986).

4. A. Facchetti, *Chem. Mater.* **23**, 733 (2011).

5. J. Kalowekamo, E. Baker, *Sol. Energy* **83**, 1224 (2009).

6. M. A. Green, K. Emery, Y. Hishikawa, W. Warta, E. *Prog. Photovolt: Res. Appl.* **20**, 12 (2012).

7. B. Kippelen, J. L. Bredas, *Energy Environ. Sci*. **2**, 251 (2008).

8. L. G. Kaake, P. F. Barbara, X. Y. Zhu, *J. Phys. Chem. Lett*. **1**, 628 (2010).

9. P. Hofmann, *Solid State Physics: An Introduction* (Wiley, Weinheim, 2008), pp. 237.

10. P. Hofmann, *Solid State Physics: An Introduction* (Wiley, Weinheim, 2008), pp. 143.

11. V. Coropceanu, J. Cornil, D. A. da Silva Filho, Y. Olivier, R. Silbey, J. L. Bredas, *Chem. Rev.* **107**, 926 (2007).

12. R. A. Marcus, *J. Chem. Phys.* **24**, 966 (1956).

13. P. F. Barbara, T. J. Meyer, M. A. Ratner, *J. Phys. Chem.* **100**, 13148 (1996).

14. V. Podzorov, E. Menard, J. A. Rogers, M. E. Gershenson, *Phys. Rev. Lett.* **95**, 226601 (2005).

15. J. D. Servites, M. A. Ratner, T. J. Marks, *Energy. Environ. Sci.* **4**, 4410 (2011).

16. N. S. Cariciftci, L. Smilowitz, A. J. Heeger, F. Wudl, *Science* **258**, 1474 (1992).

17. K. M. Coakley, M. D. McGehee, *Chem. Mater.* **16 (23)**, 4533 (2004).

18. L. G. Kaake, J. J. Jasieniak, R. C. Bakus, G. C. Welch, D. Moses, G. C. Bazan, A. J. Heege, *J. Am. Chem. Soc.* **48**, 19828 (2012).

19. H. Wang, H. Y. Wang, B. R. Gao, L. Wang, Z. Y. Yang, X. B. Du, Q. D. Chen, J. F. Song, H. B. Sun, *Nanoscale* **5**, 2280 (2011).

20. T. A. M. Ferenczi, J. Nelson, C. Belton, A. M. Ballantyne, M. Campoy-Quiles, F. M. Braun, D. C. Bradley, *J. Phy. Condens. Matter.* **20**, 475203 (2008).

21. G. Yu, J. Gao, J. C. Hummelen, F. Wudl and A. J. Heeger, *Science* **270**, 1798 (1995).

22. J. Roncali, *Acc. Chem. Res.* **42 (11)**, 1719 (2009).

23. D. Chen, A. Nakahara, D. Wei, D. Nordlund, T. P. Russell, *Nano Lett.* **11 (2)**, 561 (2011).

24. A. Kahn, N. Kock, W. Gao, *J. Polym. Sci., Part B: Polym. Phys.* **41**, 2529 (2003).

25. N. Sai, R. Gearba, A. Dolocan, J. R. Tritsch, W. L. Chan, J. R. Chelikowsky, K. Leung, X. Zhu, *J. Phys. Chem. Lett.* **3 (16)**, 2173 (2012).

26. S. Braun, W. R. Salaneck, M. Fahlman, *Adv. Mater.* **21**, 1450 (2009).

27. I. G. Hill, D. Milliron, J. Schwartz, A. Kahn, *Appl. Surf. Sci.* **166**, 354 (2000).

28. A. M. Goodman, A. Rose, *J. Appl. Phys.* **42**, 2823 (1971).

29. V. D. Mihailetchi, J. Wildeman, P. W. M. Blom, *Phys. Rev. Lett.***94**, 126602 (2005).

30. A. J. Moule, K. Meerholz, *Appl. Phys. B.* **92**, 209 (2008).

31. R. W. Boyd, *Nonlinear Optics* (Elsevier, Burlington, 2008), pp. 2

32. R. W. Boyd, *Nonlinear Optics* (Elsevier, Burlington, 2008), pp. 3

33. R. W. Boyd, *Nonlinear Optics* (Elsevier, Burlington, 2008), pp. 7

34. O. A. Aktsipetrov, A.A. Fedyanin, J. I. Dadap and M. C. Downer, *Laser Phys*. **6**, 1142 (1996).

35. K. Wu, R. Carrilies and M. C. Downer, *J. Opt. Soc. Am. B* **24**, 2736 (2007).

36. W. A. Tisdale, dissertation, University of Minnesota, 2010.

37. J. I. Dadap, dissertation, University of Texas at Austin, 1996.

38. C. J. Brabec, V. Dyakonov, U. Scherf, in *Organic Photovoltaics: Materials, Device Physics, and Manufacturing Technologies* (John Wiley & Sons, New York, 2008).

39. B. A. Gregg, *Mat. Res. Soc. Bulletin **30***, 20 (2005).

40. I.W. Hwang, Q.H. Zhu, C. Soci, B.Q. Chen, A.K.Y Jen, D. Moses, A. J. Heeger, *Adv. Func. Mater.* **17**, 563 (2007).

41. H. Ohkita, S. cook, Y. Astuti, W. Duffy, S. Tierney, W. Zang, M. Heeney, I. McCulloch, J. Nelson, D. C. C. Bradley, J. R. Durrant, *J. Am. Chem. Soc.* **130**, 3030 (2008).

42. T. Drori, C.X. Sheng, A. Ndobe, S. Singh, J. Holt, Z. V. Vardeny, *Phys. Rev. Lett.* **10**, 037401 (2008).

43. Y-H. Chen, J. Hou, S. Zhang, Y. Liang, G. Yang, Y. Yang, L. Yu, Y. Wu,; G. Li, *Nature Photonics* **3**, 649 (2009).

44. C. J. Brabec, N. S. Sariciftci, J. Hummelen, *Adv. Func. Mater.* **11**, 15 (2001).

45. H. Vasquez, R. Oszwadowski, P. Puo, J. Ortega, P. Perez, F. Flores, A. Kahn, *Europhys. Lett.* **65**, 802 (2004).

46. C. Tengstedt, W. Osikowitz, W. R. Salaneck, I.D. Parker, Che-H. Hsu, M. Fahlman, *Appl. Phys. Lett.* **88**, 053502 (2006).

47. G. Heimel, I. Salzmann, S. Duhm, J. P. Rabe, N. Koch, *Adv. Funct. Mater.* **19**, 3874 (2009).

48. S. Verlaak, D. Beljonne, D. Cheyns, C. Rolin, M. Linares, F. Castet, J. Cornil, P. Heremans. *Adv. Funct. Mater.* **19**, 1. (2009).

49. V. I. Arkhipov, P. Heremans, H. Bässler *Appl*. *Phys*. *Lett*. **82**, 4605 (2003).

50. J.-L. Bredas, J.E. Norton, J. Cornil, V. Coropceanu, *Acc. Chem. Res.***11**,1691 (2009).

51. O. Ipek, D. Veldman, S. C. G. Meskers, J. Sweelssen, M. M. Koetse, S. Veenstra, J. M. Kroon, S. S. van Bavel, J. Loos, R. A. J. Janssen *J. Am. Chem. Soc.* ***130***, 7721 (2008).

52. M. Muntwiler, Q. Yang, W. A. Tisdale, X.-Y. Zhu, *Phys. Rev. Lett.* **101**, 196403 (2008).

53. X.-Y. Zhu, Q. Yang, M. Muntwiler, *Acct. Chem. Res.* **42**, 1779 (2009).

54. L. J. A. Koster, E. C. P. Smits, V. D. Mihailetchi, and P. W. M. Blom, *Phys. Rev. B.* **72**, 085205 (2005).

55. M. M. Mandoc, W. Veuman, J. Sweelssen, M. M. Koelse, P. W. M. Blom, *Appl. Phys. Lett.* **91**, 073518 (2007).

56. C. Deibel, T. Strobel, V. Dyakonov, *Phys. Rev. Lett.* **103**, 036402 (2009).

57. H. Ishii, K. Sugiyama, E. Ito, K. Seki, *Adv. Mater.* **11**, 972 (1999).

58. W. Zhao, A. Kahn, *J. Appl. Phys.* **105**, 123711 (2009).

59. W. Osikowitz, M. P. de Jong, W. R. Salaneck, *Adv. Mater.* **19**, 4213 (2007).

60. D. S. Germack, C. K. Chan, B. H. Hamadani, L. J. Richter, D. A. Fischer, D. J. Gundlach, D. M. DeLongchamp *Appl. Phys. Lett.* **94**, 233303 (2009).

61. I. T. Suydam, S. G. Boxer, *Biochemistry* **42**, 12050 (2003).

62. L.S. Silverman, M. E. Pitzer, P. O. Ankomah, S. G. Boxer, E. E. Fenion, *J. Phys. Chem*. B, **111**, 11611 (2007).

63. S.D. Boxer, *J. Phys. Chem. B* **113**, 2972 (2009).

64. L. W. Barbour, M. Hegadorn, J. B. Asbury *J. Am. Chem. Soc.* **129**, 15884 (2007).

65. R. D. Pensack, K.M. Banyas, L. W. Barbour, M. Hegadorn, J.B. Asbury *Phys. Chem Chem. Phys.* **11**, 2575 (2009).

66. R.D. Pensack, J.B. Asbury *J. Am. Chem. Soc.* ***131***, 15986 (2009).

67. S. Qi, I. Weuts, S. De Cort, S. Stokbroekx, R. Leemans, M. Reading, P. Belton, D. Q. M. Craig, J. of Pharmaceutical Sc. **99**, 196 (2010).

68. W. Ruland, *Acta. Cryst.* **14**, 1180 (1961).

69. E. D. Gomez, K. P. Barteau, H. Wang, M. F. Toney, Y. –L. Loo, *Chem. Comm*. **47**, 436 (2011).

70. J. E. Stewart, *Infrared Spectroscopy Experimental Methods and Techniques* (Marcel Dekker Inc., New York, 1970).

71. E. S. Park, S. G. Boxer *J. Phys. Chem. B* **106**, 5800 (2002).

72. S.Middleman, A.K. Hochberg, *Process Engineering Analysis in Semiconductor Device Fabrication*, (McGraw-Hill, New York, 1993) p. 313.

73. J. Peet, J. Y. Kim, N. E. Coates, W. L. Ma, D. Moses, A. J. Heeger, G. C. Bazan, *Nat. Mater.* **6**, 497 (2007).

74. G. Li, Y. Yao, H. Yang, V. Shrotriya, G. Yang, Y. Yang, *Adv. Func. Mater.* **17**, 1636 (2007).

75. R.A. Nyquist, V. Chrzan, T. Kirchner, L. Yurga, C. L. Putzig, *Appl. Spec.* **44**, 243 (1990).

76. L. Gang, V. Shrotriya, J. Huang, Y. Yao, T. Moriarty, K. Emery, Y. Yang, *Nat. Mater.* **4**, 864 (2005).

77. M.T. Rispens,A. Meetsma, R. Rittberger, C. J. Brabec, N. S. Sariciftci, J. C. Hummelen, *Chem. Comm.* 2116 (2003).

78. H. Yang, T. T. Shin, M. –M. ling, K. cho, C. Y. Pyu, Z. Bao, *J. Am. Chem. Soc.* **127**, 11542 (2005).

79. A. S. Vadydov, *Theory of excitons*, (McGraw-Hill Book Company Inc., New York, 1962).

80. H. Sirringhaus, P. J. Brown, R. H. Friend, M. M. Nielsen, K. Bechgaard, B. M. W. Langeveld-Voss, A. J. H. Spiering, R. A. J. Janssen, E. W. Meijer, P. Herwig D. M. de Leeuw, Nature **401**, 685. (1999).

81. L.E. Alexander, in *X-ray diffraction methods in polymer science,* (Wiley-Interscience, New York, 1969) Ch.13.

82. B. J. Kim, Y. Miyamoto, B. Ma, J. M. J. Frechet, *Adv. Func. Mater*. **19**, 1 (2009).

83. W. Ma, C. Yang, X. Gong, K. Lee, A. J. Heeger, *Adv. Func. Mater*. **15**, 1617 (2005).

84. H. Hoppe, M. Niggermann, C. Winder, J. Kraut, R. Hiesgen, A. Hinsch, D. Meissner, N. S. Sariciftci, *Adv. Func. Mater*. **14**, 1005 (2004).

85. V. Shrotriya, G. Li, Y. Yao, T. Moriarty, K. Emery, Y. Yang, *Adv. Func. Mater.* **16**, 2016 (2006).

86. M.C. Scharber, D. Muhlbacher, M. Koppe, P. Denk, C. Waldauf, A. J. Heeger, C.J. Brabec, *Adv. Mater.* **18**, 789 (2006).

87. R.A. Sinton, A. Cuevas, *Appl. Phys. Lett.* **69**, 2510 (1996).

55. K.J.A Koster, V.D. Mihailetchi, P.W.M. Blom, *Appl. Phys. Lett.* **88**, 052104 (2006).

88. J. Bisquert and G. Garcia-Belmonte, *J. Phys. Chem. Lett.* **15**, 1950 (2011).

89. Y. Shen, A. R. Hosseini, W. H. Wong and G. G. Malliaras, *Chem. Phys. Chem*. **5**, 16 (2004).

90. L. J. A. Koster, V. D. Mihailetchi, H. Xie and P. W. M. Blom, *Appl. Phys. Lett*. **87**, 203502 (2005).

91. A. J. Morfa, A. M. Nardes, S. E. Shaheen, N. Kopidakis and J. Lagemaat, *Adv. Funct. Mater*. **21**, 2580 (2011).

92. G. G. Belemonte, A. Munar, E. M. Barea, J. Bisquert, I. Ugarte and R. Pacios, *Organ. Electron*. **9**, 847 (2008).

93. J. Lee, J. Kong, H. Kim, S. Kang and K. Lee, *Appl. Phys. Lett*. **99**, 243301 (2011).

94. W. Melitz, J. Shen, A. C. Kummel and S. Lee, *Surf. Sci. Rep*. **66**, 1 (2011).

95. A. Cuenat, A. Muniz-Piniella, M. Munoz-Rojo, W. C. Tsoi and C. E. Murphy, *Nanotechnology* **23**, 045703 (2012).

96. K. Wu, J. D. Canterbury, P. T. Wilson, and M. C. Downer, *Phys. Stat. Sol. (c)* **0**, 3081 (2003).

97. J. I. Dadap, J. Shan, A. S. Weling, J. A. Misewich, A. Nahata and T. F. Heinz, *Opt. Lett*. **24**, 1059 (1999)

98. T. Manaka, E. Lim, R. Tamura and M. Iwamoto, *Nature Photonics* **1**, 581 (2007).

99. H. Satou, Y. Ohshima, H. Kohn, T. Manaka and M. Iwamoto, *J. Appl. Phys*. **109**, 054506 (2011).

100. C. Lombardo, Z. Ooi, E. Danielson and A. Dodalapur, *Org. Electron*. **12**, 1185 (2012).

101. T. M. Clarke, A. M. Ballantyne, J. Nelson, D. Bradley and J. D. Durrant, *Adv. Funct. Mater*. **18**, 4019 (2008).

102. J. Hou, H. Chen, S. Zhang, G. Li and Y. Yang. *J. Am. Chem. Soc*. **130**, 16144 (2009).

103. R. W. Boyd, *Nonlinear Optics* (Acadaemic Press, San Diego, 2003), p. 42.

104. S. Cho, J. Yuen, J.Y. Kim, K. Lee and A.J. Heeger, *Appl. Phys. Let*. **90**, 063511 (2007).

105. R. I. Gearba, T. Mills, J. Morris, R. Pindak, C. T. Black, and X.-Y. Zhu. *Adv. Funct. Mater.* **21**, 2666 (2011).

106. L. Burgi, T. J. Richards, R. H. Friend and H. J. Sirringhaus, *Appl. Phys*. **94**, 6129 (2003).

107. Z. E. Ooi, K. L. Chan, C. J. Lombardo, A. Dodabalapur, *Appl. Phys. Let*. **101**, 053301 (2012).

108. H. Chen, J. Hou, A. E. Hayden, H. Yang, K. N. Houk and Y. Yang, *Adv. Mater*. **22**, 371 (2009).

109. K. R. Choudhury, J. Subbiah, S. Chen, P. M. Beaujuge, C. M. Amb, J. R. Reynolds and F. *So, Sol. Energy Mater. Sol. Cells* **95**, 2502 (2011).

110. A. Seemann, T. Sauermann, C. Lungenschmied, O. Armbruster, S. Bauer, H. J. Egelhaaf and J. Hauch, *Sol. Energy* **85**, 1238 (2011).

111. M. Lenes, H. Bolink, *Appl. Mater. Interfaces* **2 (12)**, 3664 (2010).

112. C. J. Lombadro, E. L. Danielson, M. S. Glaz, Z. E. Ooi, D. A. Vanden Bout, A. Dodabalapur, *J. Phys. Chem. B.* ASAP, (2013).

113. M. Y. Chiu, U. S. Jeng, M. S. Su, K. W. Wei, *Macromolecules*,**43 (1)**, 428 (2010).

114. C. J. Lombardo, M. S. Glaz, Z. E. Ooi, D. A. Vanden Bout, A. Dodabalapur, *Phys. Chem. Chem. Phys.* ***14(38)****, 13199 (2010).*